Department of Physics and Astronomy

University of Heidelberg

Bachelor Thesis in Physics

submitted by

Yannik Vetter

born in Schwetzingen

July 2015

Studies on charge-up effects and gain stability for the ALICE TPC upgrade with GEMs

This Bachelor Thesis has been carried out by Yannik Vetter

at the

Physikalisches Institut, Heidelberg

under the supervision of

Prof. Dr. Johanna Stachel

Abstract

The Time Projection Chamber (TPC) is the main tracking device of the ALICE detector at CERN's LHC in Geneva. During LS2 the whole readout will be replaced by Gas Electron Multiplier (GEM) detector readout to cope with the expected collision rates of about 50 kHz for Pb-Pb collisions at a design center of mass energy of $\sqrt{s_{NN}} = 2.76 \frac{\text{TeV}}{\text{nucleon}-\text{pair}}$ in Run 3. The advantage of GEM detector readout is its continuity in contrast to triggered MWPCs as they are used in the current readout. For a proper functionality the knowledge of charging-up effects inside the GEM foils is indispensable. This thesis will focus on the time it takes a detector of four GEM foils to charge completely up after ramping up the voltage and $\frac{T}{p}$ correction for the gain. It was found that during this time, in the order of 10 minutes, the gain increased by about 25% of its final value and that the charging-up time constant seems to be independent of the time (> 1 h) the detector was in stand-by mode.

Zusammenfassung

Die Time Projection Chamber (TPC) ist das Hauptelement zur Spurrekonstruktion von Teilchen im ALICE Detektor am LHC des CERNs in Genf. Während des LS2 wird die gesamte Auslese durch *Gas Electron Multiplier* (GEM)-Detektoren ersetzt, um eine Datenname bei einer erwarteten Kollisionsrate von 50 kHz für Pb-Pb Kollisionen mit einer planmäßigen Schwerpunktsenergie von $\sqrt{s_{NN}} = 2.76 \frac{\text{TeV}}{Nukleon-Paar}$ in Lauf 3 zu ermöglichen. Der Vorteil einer GEM-Detektor Auslese ist ihre Kontinuität im Gegensatz zu getriggerten MWPCs, wie sie momentan zur Auslese verwendet werden. Um ein ordnungsgemäßes Funktionieren zu gewährleisten, ist es unabdinglich, die Aufladevorgänge im Innern der GEM-Folien zu verstehen. Diese Arbeit legt ihr Augenmerk auf die Zeit, die nötig ist, um die Folien vollständig aufzuladen, nachdem die Spannung hochgefahren wurde und nach $\frac{T}{p}$-Korrektur der Verstärkung. Es wurde herausgefunden, dass während dieser Zeit, in der Größenordnung von 10 Minuten, die Verstärkung um etwa 25% ihres Endwertes zunahm und dass die Zeitkonstante des Aufladevorgangs unabhägig von der Zeit (> 1 h), die der Detektor ohne Verstärkung war, zu sein scheint.

Contents

1. Introduction

Where do we come from? This question is not only of the interest of philosophers and theologists, but also of the interest of physicists. Hence, it is not very surprising that the currently most promising theory regarding the origins of the universe - the big bang theory - was first noted by Belgian theologist and physicist Georges Lemaître in 1931 [1]. Until now, many famous physicists, like Stephen Hawking or Edwin Hubble, have contributed to this theory.
Today, physicists at the *European Organization for Nuclear Research*, CERN, in Geneva - the ALICE experiment to be more precise - try to reconstruct the events from the big bang and find out what happened in the universe just a few thousands of a billionth of a billionth of a billionth of a second (10^{-30} s) to about a millionth of a second (10^{-6} s) after the big bang. During this so called *quark-era* it is expected that quarks and gluons were nearly free particles and formed the *quark-gluon-plasma* (QGP), an extremely hot and dense state of matter. To verify this, heavy ions (lead nuclei) are accelerated in the 27 km long circular *Large Hadron Collider*, LHC, up to a few TeV and brought to collision in the ALICE detector.
One goal of the ALICE detector is to trace back the paths of the particles that were produced in the collision, identify them and check if the results match with the prediction of the quark-gluon-plasma. To do so, a huge *Time Projection Chamber*, the ALICE TPC, is one part of the detector. The coming upgrade of the ALICE TPC in 2019 includes the replacement of the MWPCs[1] with GEM[2] chambers, consisting of quadruple GEM stacks and completely new electronics for a higher readout rate which is necessary due to an increase of the collision rate to about 50 kHz.
Indispensable for a proper use of GEM detectors is a well known and stable gain and the knowledge about how to apply the high voltage to the detector without destroying the foils. Furthermore, one is interested in the time constants from the charging-up effects at the ramp up, which means, how long does it take the detector to provide stable gain after ramping up the voltage. Besides focussing on the charging-up effects, this thesis also addresses the dependence of the gain on density and water content of the gas and the ramping up of the high voltage with an *Active Voltage Divider* (AVD) which is developed in collaboration with the *RD51* [2, 3] for GEM operation.

As an outline of this thesis: a very brief physical background is introduced in section 1.1. Section 1.2 gives an overview about the accelerating process and the four big experiments. Section 2 will then focus on the ALICE detector, especially the ALICE TPC. In section 3.1 an explanation of GEM detectors will be given, how they work and what has to be taken care of. The current developments of the GEMs for ALICE will be shown in section 3.3. The main part of this thesis, the measurements and their results, are presented in section 4, respectively 4.6. As a last point a conclusion about the mean of the charging-up effects for practical implications is presented.

[1] Multi-Wire Proportional Chambers
[2] Gas Electron Multiplier

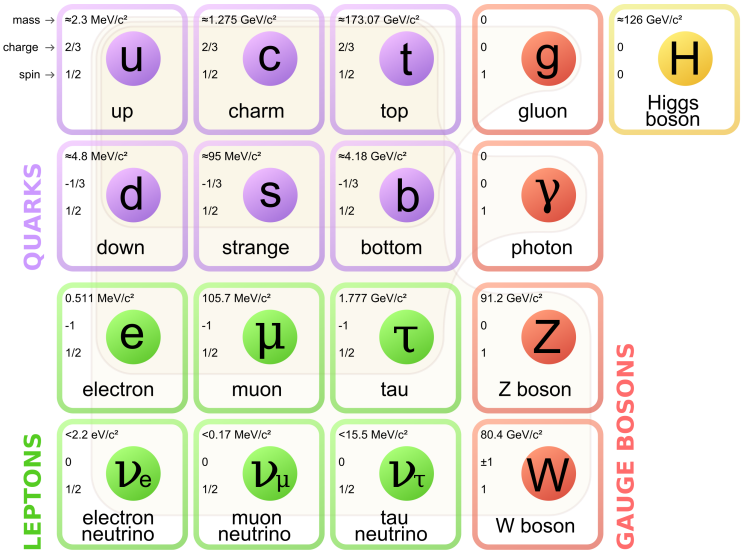

Figure 1: Three groups of particles in the Standard Model of particle physics: leptons, quarks and the gauge bosons, including the Higgs boson [5].

1.1. Physical Background

Since this thesis addresses the topic of particle detection with the ALICE TPC and especially the readout with GEM foils, I first want to take a quick look at what kinds of particles exist and how they are produced in the experiment. Therefore, the first part of this section will be about the *Standard Model* of particle physics (SM). As in particle collisions, the incident as well as the produced particles are highly relativistic a small introduction to special relativity is additionally given in the appendix.
Beginning with the Standard Model, we find a quantum field theory which combines fundamental theories, such as the electromagnetic, strong and weak interaction. However, the gravitational interaction is not included in the Standard Model. In addition, the reason for the violation of CP cannot be explained with the Standard Model. These are only two examples which show its incompleteness [4]. Nevertheless, no prediction of the Standard Model has been proven wrong so far.

Since we talk about Particle Physics, we need to take a look at the elementary particles in the Standard Model. As shown in Figure 1, the elementary particles are divided into three groups. The first group contains the six quarks and their antiparticles, the second one contains the leptons and their antiparticles and the third and last one the gauge bosons. The Higgs Boson, however, does not fit in any of these three groups. Quarks and leptons are fermions, carrying a spin of $1/2$, whereas the gauge bosons have spin 1. Further the gauge bosons are the mediators in the interactions: photons for the electromagnetic, gluons for the strong and $W^{\pm}$ and Z for the weak. Plus, leptons only participate in electromagnetic and weak interaction, whereas quarks can also participate in strong interaction. In contrary to leptons, which can exist without any other lepton, like an electron in a hydrogen atom, quarks form other particles. They are the constituents of the hadrons, such as protons, neutrons (both are examples for baryons; three quark particles) or pions (as an example for mesons; two quark particles).

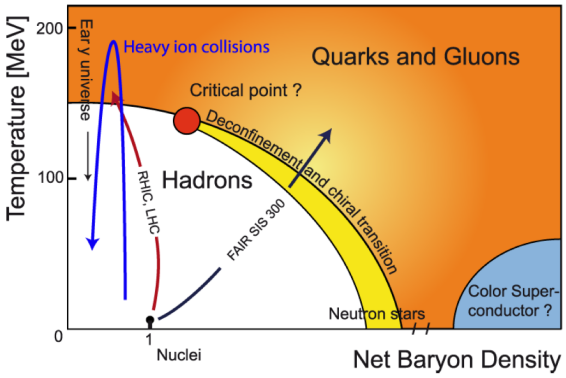

Figure 2: QCD phase diagram; the white region shows hadronic matter, the orange region shows the QGP; adapted from [7].

According to Quantum Chromodynamics (QCD), which explains the strong interaction, the quarks carry a color (anticolor for antiquarks, respectively): red, blue and green (antired, antiblue and antigreen for the antiquarks). Analogous to charge neutrality in atoms, color neutrality is required for hadrons. However, quarks carry only one color each, which means they cannot exist in unbound states. QCD also predicts phase transitions in the QCD phase diagram (see Figure 2) from hadronic matter to the QGP. The diagram shows the temperature in MeV[3] against the baryonic chemical potential μ_B, which refers to the baryon density. Under less extreme conditions we find hadronic matter, or so called confined matter, in which quarks and gluons bind and form hadrons. Under extreme conditions, as they have been very shortly after the big bang, we cross the critical point (red dot; not sure, if it really exists [6]) and enter the regime of the quark-gluon-plasma. In this state of matter, quarks and gluons are assumed to be nearly free particles. This state is also called deconfined matter.

In the ALICE experiment at the LHC at CERN, Geneva, physicists want to reproduce and probe this state by colliding two lead nuclei at a center of mass energy of $\sqrt{s_{NN}} = 2.76 \frac{\text{TeV}}{\text{nucleon}-\text{pair}}$, thus reaching the necessary temperature and baryon density. As the QGP cools down, the process of hadronization can be observed, meaning the transition from nearly free quarks and gluons to color neutral, bound hadronic states like protons and pions.

1.2. The LHC at CERN

Up to 100 m below the surface, the world's largest particle accelerator - CERN's Large Hadron Collider - is located along the border between France and Switzerland. Currently proton-proton collisions at a center of mass energy of $\sqrt{s_{NN}} = 13\,\text{TeV}$ for Run 2 are prepared. The energy is almost twice as high as during the first runs, starting in 2008. To achieve these kinds of energies a circular accelerator is essential; being of 27 km of length in the case of the LHC.
Four big experiments are placed along the LHC ring: ATLAS, CMS, LHCb and ALICE.

[3] $\frac{1\,\text{eV}}{k_B} = 11604.505\,\text{K}$

Table 1: About the LHC [8, 9].

Quantity	**number**
current in bending dipole magnets	11 850 A
mass of accelerated protons	2 nanograms
speed of protons	0.999999991 c = 299 792 455.302 m/s
data taken per year	∼ 15 PB (=15 000 000 GB)
energy per proton beam	equivalent to 400 t train (ICE or TGV) at 150 km/h
beam pressure	$\sim 10^{-13}$ bar (ultrahigh vacuum)
energy consumption	800 000 MWh (in 2009)
cost	∼ 5 billion CHF for the LHC

Table 2: Parameters of the LHC; adapted from [8].

Quantity	number
Circumference	26 659 m
Dipole operating temperature	1.9 K (-271.3°C)
Number of magnets	9593
Number of main dipoles	1232
Number of main quadrupoles	392
Number of RF cavities	8 per beam
Nominal energy, protons	7 TeV
Nominal energy, ions	2.76 TeV/u (*)
Peak magnetic dipole field	8.33 T
Min. distance between bunches	~7 m
Design luminosity	10^{34} cm^{-2} s^{-1}
No. of bunches per proton beam	2808
No. of protons per bunch (at start)	1.1×10^{11}
Number of turns per second	11 245
Number of collisions per second	600 million

(*) Energy per nucleon

Some details about the LHC will be given in the following paragraphs.

The LHC is the biggest and most expensive machine ever built by mankind. Some important parameters are presented in tables 1 and 2.

Before the injection into the LHC, the protons (Pb ions) are pre-accelerated, which is done in four smaller accelerators, namely LINAC2/3, PSB, PS and SPS.
At the very beginning, there is a hydrogen gas bottle from which a specific number of hydrogen atoms is taken. The H-atoms are ionized by passing through an electric field [10] such that only protons are remaining. Those protons are accelerated by radio frequency quadrupoles (RFQ)[4] which first attract the protons until they pass through them, then change their polarity and repel the protons [11]. This process is repeated throughout the LINAC[5]. At the end the energy of the proton beam is about 50 MeV.
From the LINAC2 the protons are injected into the *Proton Sychrotron Booster* (PSB) where they are accelerated to 1.4 GeV [12]. The acceleration is done in the same way as in the LINAC2, except that the PSB consists of four stacked rings with circumference of

[4] electric quadrupoles to accelerate and magnetic quadrupoles to form the beam
[5] note that the distance between the quadrupoles increases because the speed of the particles increases and the radio frequency stays the same

about 157 m each [13].
The next step is the *Proton Synchrotron* (PS) which also is a circular accelerator with circumference of about 600 m . The energy of the beam at the end is 25 GeV [14].
At this energy the beam is injected into the *Super Proton Synchrotron* (SPS) which has a circumference of about 7 km [15]. Again the same accelerating mechanism is used and thus, the beam energy is increased to 450 GeV [8].
The last step of the acceleration procedure is the injection into the 27 km long LHC ring, where the energy is increased to its final value (currently 6.5 TeV for proton beams). Note that the whole procedure is done for two separate beams which are accelerated in opposite direction, one beam clockwise, the other one counter-clockwise. To prevent the beams to collide randomly two different tubes are used, one for each beam. At the four collision points (the four big experiments) the beams are brought together with magnets.
The acceleration of 2 nanograms of hydrogen takes about 20 minutes until the energy of 6.5 TeV is reached. [8] For heavy ion collisions lead is used. There are only small differences in the accelerating procedure: at the beginning lead is evaporated and ionized to Pb^{27+}, then injected into LINAC3 and then into LEIR (*Low Energy Ion Ring*) - instead of PSB - where the the bunches are shortened. The next steps are the same, but the energies at the end are different and in the PS the remaining electrons are stripped from the ions until they become Pb^{82+} [7]

ATLAS is the acronym for *A Toroidal LHC ApparatuS* [16, 17] and is a 46 m long and 25 m high detector. Its research covers the search for new particles, dark matter, supersymmetry, extradimensional space and confirmation of the standard model.
The discovery of the Higgs boson in 2012, together with CMS, was the latest and probably greatest accomplishment by now.

The *Compact Muon Solenoid* (**CMS**) [18] experiment is of general purpose. It covers a large range of research beginning from the search for new particles and confirmation of the standard model to the search for potential dark matter particles.
The detector contains the biggest superconducting solenoid magnet in the world and weights about 14 000 tons.
Due to the high magnetic field created by the solenoid, the flight paths of charged particles are bent. The high field is necessary because the bending radius decreases with increasing momentum of the particles. Thus, it is easier to measure the momentum of particles and identify them in this way.

The *b* in **LHCb**[19] stands for beauty, which refers to the purpose of the detector, the measurement of B-meson[6] decays.
Compared to the other three big LHC experiments, the LHCb detector has no cylindrical shape. The reason for this different design is that the produced B-mesons stay close to the beam line, which means there is no need in particle detection in big distances from the beam line. Therefore the LHCb subdetectors are built along the beam line, like a stack of papers.

[6] particles containing b quarks ($\bar{b}$ respectively)

2. ALICE - A Large Ion Collider Experiment

The ALICE experiment [20] is the only one of the four big experiments at the LHC designed to study heavy ion - particularly Pb-Pb - collisions. In these collisions quark-gluon-plasma (QGP) is produced.
In addition to that, ALICE can also be used in p-p- and p-Pb-collisions.[7]
The whole experiment consists of several detectors built in a 26 m long, 16 m high and 16 m deep solenoid magnet[8] with a field of 0.5 T. Fig. 3 shows the ALICE experiment with its detectors and the L3 solenoid magnet (9). To name the biggest ones from the interaction point outwards: **I**nner **T**racker **S**ystem (ITS; 1), **T**ime **P**rojection **C**hamber (TPC; 3), **T**ransition **R**adiation **D**etector (TRD; 4), **T**ime **O**f **F**light (TOF; 5), **H**igh **M**omentum **P**article **ID**entification (HMPID; 6), **E**lectro**M**agnetic **CAL**orimeter (EMCAL; 7), and the **PHO**ton **S**prectrometer (PHOS; 8). In this thesis the focus will be on the TPC, for which an upgrade to GEM detector readout is planned.

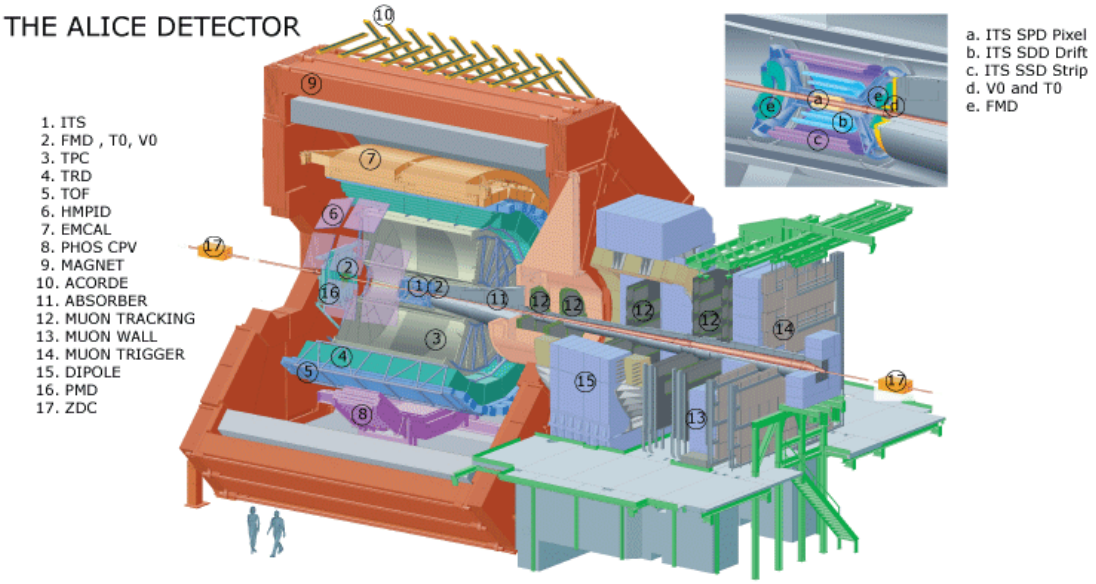

Figure 3: The ALICE experiment [21].

An overview of the TPC, how it is built, how it works and what the update to GEM detector will change, is given in section 2.1. A short introduction to the other subdetectors will be given in the following paragraph.

Starting at the interaction point and going outwards, as above, the ITS is the innermost subdetector and consists of different silicon detectors which cover the full azimuth, a rapidity region of $|\eta| \leq 0.9$ and are placed up to radius of about $r = 45\,\text{cm}$ in six layers. Its purpose is the reconstruction of the primary vertex and secondary vertices, particle identification and tracking of low-momentum particles [20].
The next layer is the TPC, from $r = 84.8\,\text{cm}$ to $r = 246.1\,\text{cm}$.

[7] ATLAS and CMS also measure heavy ion collisions, but it is not their main purpose
[8] L3 magnet; leftover from LEP

Further outwards the TRD [22] is installed, also covering the full azimuth and a rapidity region of $|\eta| \leq 0.9$. It is composed of 18 supermodules surrounding the TPC, each consisting of 30 read-out chambers (five stacks, six layers). The working principle is based on transition radiation caused by electrons in the energy region of about 0.5 to a few GeV/c^2. The photons deposit their energy of around 10 keV in the drift area of the respective read-out chamber, which is filled with a Xe-CO_2 (85-15) gas mixture. The TRD is used for identification of electrons and as a high p_T trigger.
Next is TOF, also covering full azimuth. It is used for particle identification by measuring the time of flight of the respective particles. The layers above TOF do not cover the whole azimuth, but consist of two subdetectors. First one comprises the EMCAL and the HMPID, the second one only PHOS, which is placed on the bottom of the inside of the L3 magnet. The purpose of HMPID is particle identification of high momentum particles. In PHOS direct photons are detected using lead-tungstate crystals ($PbWO_4$) and the EMCAL is used to determine the energy of particles underlying the electromagnetic interaction, such as electron or gamma rays.
Outside the central barrel, there is a muon tracker and other subdetectors used as a trigger. The muon tracker [23] measures muon pairs produced in the decay of quarkonia like J/ψ. It is located on the C-side of ALICE and consists of an absorber, made from lead, boronated polyethylene, tungsten, carbon and concrete in an order to minimize multiple scattering, which is located inside the L3 magnet to extract most non-muon particles, five trackers and the *Fass* dipole magnet, both outside the L3 magnet.

2.1. The ALICE TPC

The overall idea of a TPC in general is to reconstruct a three dimensional trail of charged particles and to determine their energy loss per length $\frac{\mathrm{d}E}{\mathrm{d}x}$, from which the particles can be identified, by ionization of a gas. The most common form of a TPC is a sealed cylindrical container, filled with a working gas and surrounded by a magnet which provides a homogenous field inside the container in which the tracks of charged particles are bent and from which their momentum can be determined. On one side a high voltage electrode is located and on the other side readout chambers are mounted. A particle traversing the gas volume of a TPC ionizes the gas atoms or molecules, depending on the working gas, along its path and leaving electron-ion-pairs behind. By applying a drift field, which is an electric field from the drift cathode to the readout chambers parallel to the magnetic field, these electron-ion-pairs are separated and the ions drift towards the cathode and the electrons towards the readout chambers. To reconstruct the track of a particle, the readout chambers deliver information about the two dimensional track in the $r\varphi$ plane and by measuring the time difference between the detection of a signal on the readout and a reference time, the z-coordinate can be determined. For the latter, the knowledge on the drift velocity of electrons in the respective working gas is of necessity.
Further, the amount of electrons liberated in the passage of the particle can be translated into the energy it has lost along its track. From the reconstructed track, the path length can be determined and therefore the energy loss per length, which is needed to identify the

particle. A more detailed view on the ALICE TPC is given in the following paragraphs.

The ALICE Time Projection Chamber [20, 24, 25, 26] is the largest of its kind. It is a hollow cylinder with a diameter of 5 m, a length of about 5 m and an active gas volume of about 90 m^3. Figure 4 shows a schematic of the ALICE TPC. As can be seen in the middle of the cylinder, a central high voltage (HV) electrode divides the gas volume into two equal smaller volumes and on the endplates the readout is mounted. Both endplates are composed of 18 trapezoidal sectors, each consisting of an *outer readout chamber* (OROC) and an *inner readout chamber* (IROC). The current readout uses Multi-Wire Proportional Chambers (MWPCs). Overall, the ALICE TPC readout contains $2 \times 18 = 36$ IROCs and OROCs with more than half a million readout pads [24].
The voltage applied to the central high voltage electrode is 100 kV, thus creating an electric field of 400 V/m pointing towards the electrode. This electric field is the drift field, in which electrons - produced in ionizing processes - drift towards the endplates where the readout hardware is mounted. This is shown by an exemplary track inside the active volume with electron-ion-pairs and their drift direction indicated. It is essential that the drift field is as homogenous as possible. This is ensured by a field cage. If the drift field would suffer from inhomogeneities, the time information from the electrons would not be reliable anymore and the z position can be distorted. Thus it would be almost impossible to measure the particle's momentum[9]. The field cage comprises of strips placed on the inner and outer side of the vessel along the drift volume. To each strip a potential is applied using a resistor rod, which decreases towards the readout chambers.

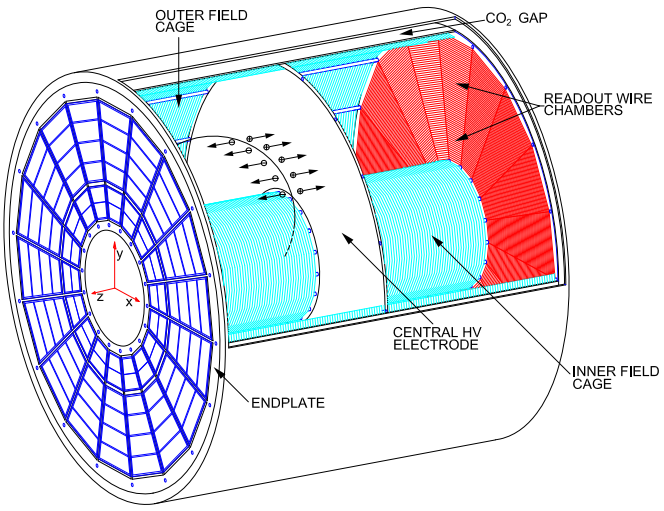

Figure 4: Schematic of the ALICE TPC showing the field cages (cyan), the end plates (red inner side, blue outer side) and the central HV electrode [27].

Figure 5 shows the electric field lines and the lines of equipotential for a schematic view on two strips. The strips are indicated on the left side, middle respectively, of the pictures. In figure 5a the pitch Δ between two strips is shown. Besides, figure 5b shows a symmetric view on the field lines and equipotential and one can see how the lines of equipotential are squeezed between the two strips and that the electric field lines are always perpendicular

[9] at least a very precise knowledge of the field lines would be necessary to perform elaborate corrections

to them. The lines of equipotential result from the decreasing potential on the strips. The field between two strips, now, is formed as mentioned before. This means, the electric field lines reach from one strip to the next. The superposition of the field created by the cathode and the fields between the strips is almost homogenous, as can be seen in figure 5b. The pertubation of the field at a distance equal to the pitch Δ is only in the order of 10^{-3}. The pitch between two strips in the ALICE TPC is 15 mm, which means, the field is completely homogenous compared to a radius of 160 cm from the inner boundary to the outer. In order to protect the rest of the experiment from the high voltage applied to the field cage a CO_2 filled gap is implemented between the outer shell of the TPC and the field cage, as be seen in figure 4.

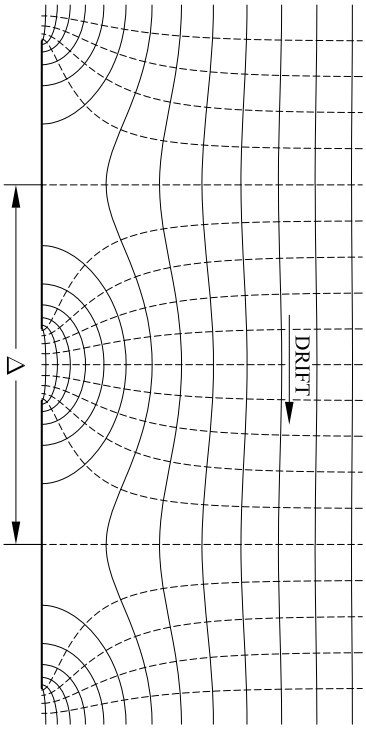

(a) Schematic of function of the field cage.

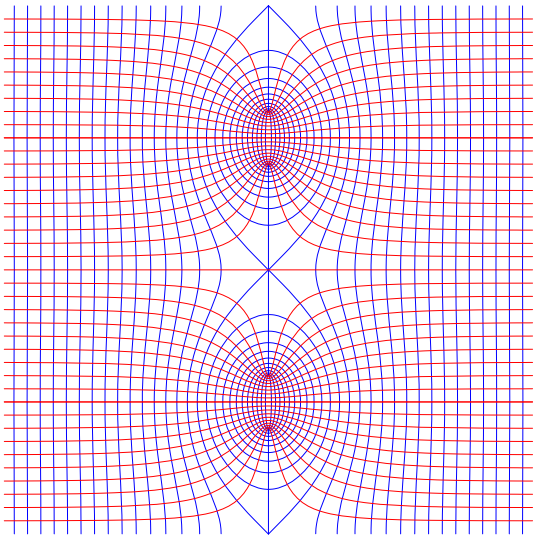

(b) Electric field lines (blue) and equipotential lines (red); the strips are also shown in blue as straight vertical lines.

Figure 5: Simulation of the field lines and lines of equipotential for two strips of the field cage [27].

Since the ALICE TPC uses gas ionization to track and identify particles it is indispensable that the whole vessel is gas tight which is realized by using Tedlar foil.
The gas used in the ALICE TPC is a mixture of neon, carbondioxide and nitrogen, at nearly atmospheric pressure[10]. In order to save gas it is recirculated at a flowrate of 15 m^3/h. Some of the gas is exhausted, though, or taken out of the cycle for analysis on oxygen and water content or mixture controlling with a gas chromatograph to assure the quality. The reason why oxygen and water content are controlled regularly is the unwanted property of oxygen atoms to attract and bind electrons (produced in the ionization process) which, hence, can no longer drift to the readout chambers and be detected. Due to this continuous

[10] the pressure is 0.5 mbar higher than atmospheric pressure

outtake of gas, 50 l/h are added.
The gas mixture contains the working gas, neon, as well as two quencher gases in order to limit the ionization. Commonly, hydrocarbons are used as quenchers, but due to their poor longterm stability they are unsuitable. Another possibility would be CF_4 which also has positive effects on other characteristics of the gas. The compatibility with some materials used in the TPC brought up concerns, though, which is the reason why CO_2 was chosen instead. The amount of 10% results from design parameter such as the total drift time.

2.2. Particle Tracking with the ALICE TPC

The particles produced in the collisions pass through the active volume of the ALICE TPC and interact with the working gas. Some of these interactions lead to ionization. Since only a fraction of the particles energy is necessary to ionize a neon atom, it will continue its way through the gas and ionize further atoms. This means, along its track atoms are ionized and ions and electrons are separated. Due to the electric field inside the chamber, the ions drift towards the central HV electrode and the electrons drift towards the endplates with the readout chambers. With the knowledge about the electric field inside the chamber as well as of the drift velocities and mobilities of the ions and the electrons in the gas mixture, it is now possible to calculate where the ionization process took place in the z-direction. This is done by measuring the time of the arrival of the electron on the readout compared to a reference time, like the start of the collision. Since particles produced in collisions in accelerators are highly relativistic it takes them a few nanoseconds to traverse through the gas volume, in contrast to several tens of microseconds of drift time. Because of this, it is not necessary to differ between the start times of the drift of the electrons. They are assumed to be coincident.
To determine the x and y coordinate of the track the pad readout is used. After the electrons have drifted through the gas they enter the readout chambers. In them, the electrons are multiplied to be able to measure a current, since the measurement devices always have some noise and therefore are not able to detect arbitrarily small currents down to the order of single electrons. This amplification is currently done by MWPCs and after the upgrade in 2018 it will be done with GEMs. The pads of the pad readout have three different sizes: $4 \times 7.5\,\mathrm{mm}^2$ $(r\varphi \times r)$ for the IROC, $6 \times 10\,\mathrm{mm}^2$ $(r\varphi \times r)$ $(1346 < r < 2066\,\mathrm{mm})$ for the inner of the OROC and $6 \times 15\,\mathrm{mm}^2$ $(r\varphi \times r)$ $(2086 < r < 2461\,\mathrm{mm})$ for the outer of the OROC [24]. With the *front end electronics* (FEE) the pads are read out and it is possible to read each pad separately. Thus the x and y coordinate - $r\varphi$ and r, respectively - are determined.
The spatial resolution depends on the pad size and the diffusion on the electrons in both the drift volume and the amplification area. Currently it is in the order of 0.1 to 1 cm in the $r\varphi$ plane and will not deteriorate by more than 10% for GEM readout. The accuracy for the z-coordinate is slightly lower, but in the same order of magnitude.
The drift velocity $\mathbf{u}$ of electrons in an electric and magnetic field is given by [28]

$$\mathbf{u} = \frac{e}{m}\tau E \frac{1}{1+\omega^2\tau^2}\left(\hat{\mathbf{E}} + \omega\tau\left(\hat{\mathbf{E}}\times\hat{\mathbf{B}}\right) + \omega^2\tau^2\left(\hat{\mathbf{E}}\cdot\hat{\mathbf{B}}\right)\hat{\mathbf{B}}\right) \quad (1)$$

where $\hat{\mathbf{E}}$, $\hat{\mathbf{B}}$ represent the unit vectors of the fields, $\omega = \frac{e}{m}|\mathbf{B}|$ the cyclotron frequency and $\tau = \frac{m}{K}$ with m the mass of the particle and K a parameter describing the frictional force in the gas. Equation 1 reduces to $\mathbf{u} = \mu \cdot \mathbf{E}$ for $\mathbf{E} \times \mathbf{B} = 0$ with μ as the mobility of the electrons in the respective gas.
However, the magnetic field of the solenoid magnet is not perfectly homogenous and therefore not always parallel to the electric field inside the TPC. This results in $\mathbf{E} \times \mathbf{B} \neq 0$ which means the drift path of the electrons is distorted. The distortions in the ALICE TPC due to this $\mathbf{E} \times \mathbf{B}$ - effects are in the order of 1 cm, depending on the z coordinate.
Now that one knows the track of a particle and further the magnetic field strength, one can determine the momentum of the particle from the bending radius of its track.

2.3. Particle Identification

Besides particle tracking the ALICE TPC is also used for *particle identification* (PID). For proper identification the charge and the mass have to be determined. The sign of the charge can be determined by the direction of the radius of the curvature in the magnetic field inside the L3 magnet. To specify the mass of the respective particle one has to perform more complicated measurements. For one, the momentum of the particle has to be determined from the radius of the curvature according to $p = 0.3qBr$ with $q = ze$ the charge in multiples of the elementary charge, B the magnetic field strength in Tesla, r the radius of the curvature in meters and 0.3 a scaling factor to obtain p in GeV/c. In addition to that $\beta\gamma$ is extracted from the energy loss $\frac{\mathrm{d}E}{\mathrm{d}x}$. This can be done, since during the passage of a particle through matter [29], it loses energy in different processes, depending on its energy. For intermediate particle energies, the main energy loss process is due to ionization. Table 5 in Appendix A.2 shows the contribution of the different processes to the total energy loss for muons in argon. In this particular case the main energy loss for muon energies up to about 100 GeV is due to ionization. Above this energy radiation effects have to be considered.
The mean energy loss per length for heavy particles[11] is described by the *Bethe-Bloch*-formula [29]:

$$-\left\langle\frac{\mathrm{d}E}{\mathrm{d}x}\right\rangle = \frac{4\pi N_A e^4 \varrho}{m_e c^2}\frac{Z}{A}\frac{1}{\beta^2}z^2\left[\frac{1}{2}\ln\frac{2m_e c^2\beta^2\gamma^2 T_{max}}{I^2} - \beta^2 - \frac{\delta(\beta\gamma)}{2}\right] \quad (2)$$

where N_A is the Avogadro number, ϱ the (gas) density, $m_e c^2$ the rest energy of the electron, $\frac{Z}{A}$ the ratio between atomic number and weight, z the charge number, T_{max} the maximum transferred kinetic energy, I the mean excitation energy and $\delta(\beta\gamma)$ a correction made for the so-called density effect.

[11] particles with mass much higher than electrons

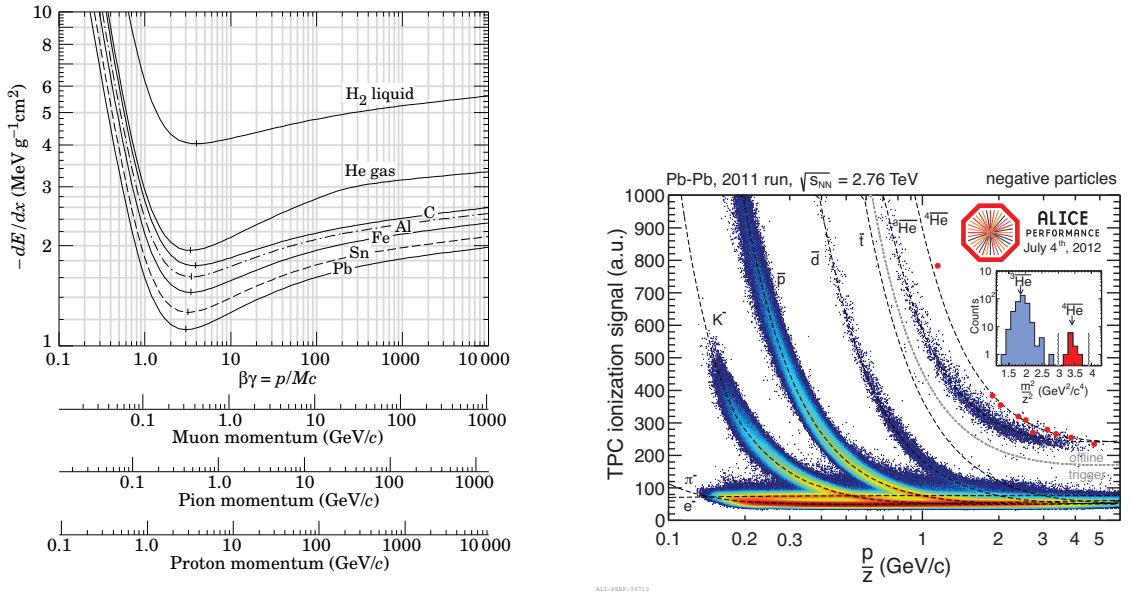

(a) **(b)**

Figure 6: Energy loss $\frac{\mathrm{d}E}{\mathrm{d}x}$ as a function of the $\beta\gamma$ for different materials (left), adapted from [29]; same plot created with measurements from the ALICE TPC (right), by A. Kalweit, CERN (2011).

Equation 2 shows a minimum at $\beta\gamma \simeq 3$, shown in figure 6a, from which the mass of a particle can be determined, since $\beta\gamma = \frac{p}{Mc}$, where M is the particles mass and p its momentum which is determined by the curvature radius of its track as mentioned before. Particles, which show energy losses near the minimum are therefore called *minimum ionizing particles*, MIPs.

Above a certain transfer of kinetic energy, T_{cut}, so called δ -rays are produced, which are secondary electrons with high energy. One downside of δ-electrons is, that they lead to a smeared track, since they cannot always be assigned to the original track of the particle.

Further, the energy loss described by the Bethe-Bloch formula (eq. 2) is the mean value of the energy loss distribution, which is a *Landau* distribution. It shows how often a certain energy loss occurred. This means, the distribution has a Gaussian like shape, but with a tail towards high energies which is due to δ electrons. This means one has to distinguish between the actual energy loss, the mean energy loss given by equation 2 and the most probable energy loss, which is the maximum of the Landau distribution.

But how is the energy loss determined in the ALICE TPC? By measuring the current on the readout for one track and with the knowledge of the gain of the GEMs - or currently the MWPCs - it is possible to determine the total energy a particle has deposited along its path through the gas volume. Since almost all particles are considered to be MIPs, their energy loss stays almost the same throughout their whole track. The spatial reconstruction of a track yields the path length and therefore $\frac{\mathrm{d}E}{\mathrm{d}x}$ can be obtained. For one track, one gets the Landau distribution of $\frac{\mathrm{d}E}{\mathrm{d}x}$. By truncating the highest $\sim 30\%$ are removed, which complies with the tail of the distribution. Then the mean value of the remaining distribution is calculated and plotted against the momentum of the particle. With increasing number of particles plotted in the same diagram, the shape of the Bethe-Bloch formula forms. Figure

6a shows the theoretical shape of the Bethe-Bloch formula and figure 6b the respective plot obtained from the TPC. The identification of the particle then is done by comparing the two plots, naively speaking. For example, if a measured track yields an energy loss of 300 with a momentum of $p/z = 0.2\,\mathrm{GeV}/c$ the particle can be identified as a K^- in figure 6b, since there is no ambiguity. As can also be seen, not all particles can be considered to be MIPs, since the ones showing no ambiguity are in the region left to the minimum.
As one can see, it is very difficult, if not impossible, to determine the difference between pions and electrons. To avoid misidentifications, the ALICE TRD identifies electrons, such that the TPC can identify pions.

3. Gaseous Detectors

In general gaseous detectors are used for particle tracking and particle identification due to energy-loss $\frac{\mathrm{d}E}{\mathrm{d}x}$ or other processes like Cherenkov or transition radiation. The underlying principle is the passage of particles through matter, gases in this particular case. For example, a pion traverses the active gas volume of a detector. Along its path, it ionizes the gas atoms (or molecules, depending on the used gas) and thus loses energy according to the Bethe-Bloch formula (eq. 2). The number of primarily produced ionization electrons per unit length is given by the *first Townsend coefficient* α[30, 31]. During this process produced ionization electrons and positive ions are separated in an electric field and drift towards the respective electrodes. Depending on the energy transfer during the primary ionization process, the ionization electrons might also have enough energy to ionize gas atoms/molecules along there path themselves, called secondary ionization [32]. If the electric field is high enough to accelerate the electrons up to energies greater than the energy necessary to ionize the gas atoms/molecules avalanches form. This is the case very close to the anode wires for MWPCs or inside the holes for GEMs, as it is explained in the next section. Therefore, at the path of the traversing particle one primary electron is produced and at the anode multiple electrons arrive.
For the reconstruction of the path of the traversing particle, the pion in the example above, a readout for the electrons is of need. Since their number is very small, the acquired signal is also very small, if even measurable. Therefore it is helpful to amplify the signal by, for example, increasing the number of electrons reaching the readout. One possibility to do so is by using a gas electron multiplier, so called GEM, which is described in the following section.

3.1. Description of Gas Electron Multiplier

The gas electron multiplier (GEM) was introduced by Fabio Sauli, in 1997 [33] and can be classified in the area of micropattern gaseous detectors (MPGDs). It consists of a $50\,\mu$m thin, insulating polyimide layer (Kapton[12] in this case) covered with copper ($2-5\,\mu$m) on both sides on which the voltages are applied to. This foil is placed inside a gas container and is flushed with gas. Throughout the foil holes are etched into it with a double conical[13] shape resulting from the chemical etching process. The pitch of the holes varies from $70\,\mu$m for small pitch foils to $280\,\mu$m for large pitch foils. The holes have about $50\,\mu$m of inner diameter and about $70\,\mu$m of outer diameter and are arranged in a hexagonal pattern. Figure 7 shows a microscopic view of a GEM foil. One can clearly see the conical shape of the holes and the layers of which the foil consists (copper, Kapton, copper). The foils are pre-stretched and fixed in a frame. This is due to electrostatic effects. As soon as a voltage is applied to the foil, an electric field is created. If two foils are superimposed in a detector, electrostatic forces attract them. To avoid a short circuit resulting from the two foils touching each other, they need to be stretched and put into frames to keep the tension.

[12] Kapton is a registered trademark of DuPont
[13] in the following sections conical will always refer to double conical shape

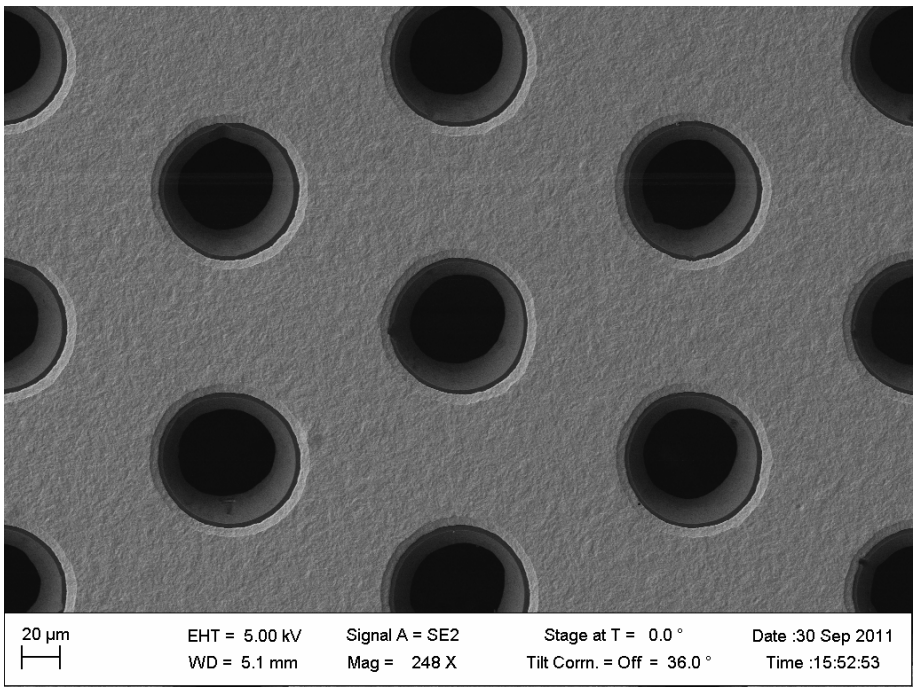

Figure 7: Microscopic view of a GEM foil; the conical shape of the holes is clearly visible as well as the different layers; adapted from [24].

The GEM foils used in the experiment have an active area of $10 \times 10\,\mathrm{cm}^2$ and were produced at CERN.
Coarsely speaking, a GEM foil embodies a simple plate capacitor with a dielectric medium in between the plates. The difference to the simple plate capacitor are the holes in the GEM foil. A modest way to calculate the capacitance of one foil is to assume there are no holes. The capacitance for a plate capacitor is computed by:

$$C = \varepsilon\varepsilon_0 \frac{A}{d} \tag{3}$$

where ε is the dielectric constant, $\varepsilon_0 = 8.85 \cdot 10^{-12}\,\mathrm{F/m}$ the vacuum permittivity, A the area of the plates and d their distance. The dielectric constant for $d = 50\,\mu\mathrm{m}$ Kapton foil is $\varepsilon = 3.4$ [34]. This yields a capacitance of $C \simeq 600\,\mathrm{pF}$ per foil.

As mentioned above, an electric field builds up when a voltage is applied to the two sides of the GEM foil. Figure 9 shows the field lines inside a hole of a GEM foil. One can see that the field lines (from left to right) inside a hole are very dense which implies a very high electric field of $\mathcal{O}(50\,\mathrm{kV/cm})$. The force on a charge in an electric field is given by $F = qE$ and thus big for high fields. Accordingly, charges are accelerated more in higher fields and gain more energy. In the case of GEMs the charges are carried by electrons and ions. As soon as an electron, created by primary ionization processes, is accelerated and has gained enough energy to ionize a gas atom, the ionization takes place and an electron-ion-pair is produced. This process occurs multiple times, since more electrons produced by primary ionization drift into the hole. Also secondary ionization occurs, as

soon as the secondary electrons have gained enough energy from the field inside the hole. Thus an avalanche forms. It is obvious that the amount of electrons produced inside a GEM foil due to ionization is depending on the applied voltage. Higher voltage leads to a higher number of produced electrons and hence higher gain. After the amplification, the electrons can be read out. This is done by a readout anode, for example made out of read out pads, called *pad plane*, like it will be used for the ALICE TPC. The effective gain can be considered as the ratio between the current without amplification, measured before the foil, and the current with amplification,measured on the anode, which means:

$$G_{eff} = \frac{I_{amplification}}{I_{no\,amplification}} = \frac{I_{pad\,plane}}{eN_{ion}R} \tag{4}$$

where e is the elementary charge, N_{ion} the total number of ionization electrons per one incident particle and R is the rate of the incident particles. Its dependence on the applied voltage is exponential as can be seen in figure 8. There are different effects that decrease the theoretical gain of GEM foil, which is the reason why it is referred to as the effective gain. Some of these effects will be discussed later in this section. However, the gain (both theoretically computed and effective) do not rise to infinity, even if they show an exponential increase with voltage. The limit to the value of the gain is on the one side the occurrence of discharges and on the other side the *Raether-Limit* $G_{Raether} \approx 2 - 6 \cdot 10^6$ [35]. This limits gives the number of electrons at which a discharge occurs and refers to a single incident electron on a single GEM foil.

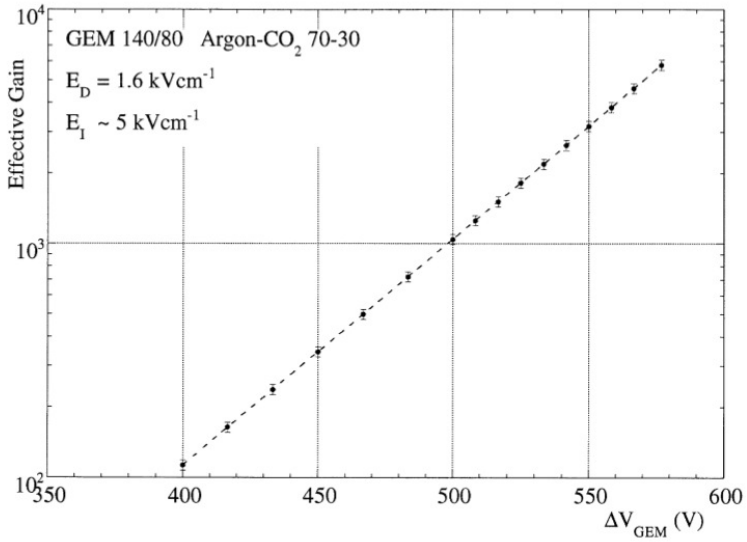

Figure 8: Dependence of effective gain and applied voltage; conditions in top left corner; adapted from [36].

Further, during the ionization and amplification process created, ions and electrons drift along the electric field lines, ions towards the upper side of the GEM foil and electrons towards the lower side of the foil. After the ions leave the hole most of them are collected on the upper copper layer of the foil because they closely follow the electric field lines due

to small diffusion. Some of them drift into the drift volume. Ideally, all ions would be gathered from the top side of the GEM foil since the ions that drift back into the drift volume create space charges which distort the electric field. The fraction of the ions drifting back is quantified by the *ion backflow IBF* and amount to less than 1% for the ALICE TPC GEM readout according to the TDR.
The electrons created in the avalanche have a higher diffusion and may therefore reach the surface of the insulating Kapton layer inside the hole, although no electric field lines originate or end on the dielectrics surface. These electrons can then attach to the Kapton and accumulate on its surface due to polarization effects, which leads to a charging-up of the GEM itself, which is the main topic of this thesis. This charging-up leads to a change in the electric field due to screening effects. However, the effects of charging-up on a microscopic level are not fully understand, yet, but are observed experimentally. This means, the above given explanations are the most common ones and mainly accepted, but not yet proven.

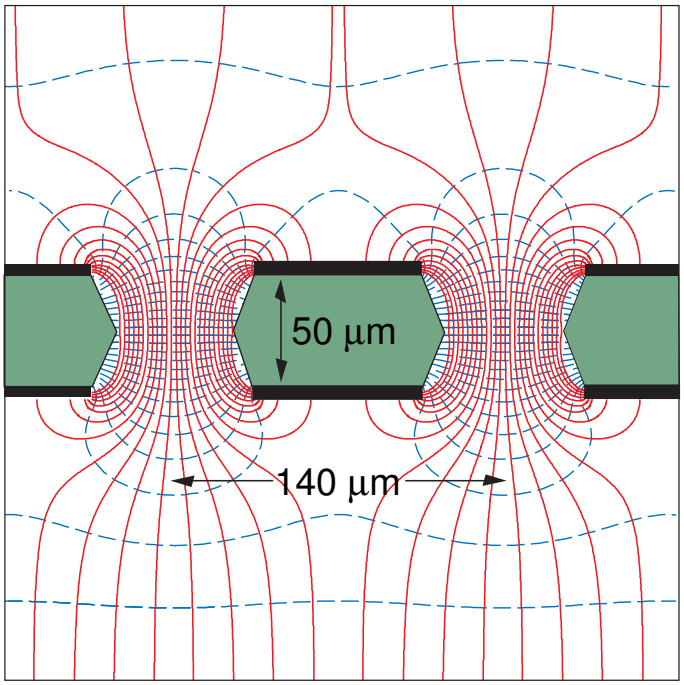

Figure 9: Vertical view on two holes of a GEM foil with equipotential (dashed blue) and the most inner electric field lines (red) inside the hole; adapted from [37].

There are several parameters which influence the time it takes until a foil is fully charged up and the amount of charge stored inside the holes. Previous works [38, 39] show, that these parameters are irradiation rate and water content of the working gas as the most important ones. The transferability of these results must not be given, since several different settings are possible. However, it is assumed that the overall dependence on these parameters is very similar for all setups which gives a rough expectation for the results of this work.
Another dependence of the charging-up time is how long the foils have not been exposed

to radiation, how long they were able to discharge[14]. This is a very trivial parameter, since for short cool down times more charges are still accumulated on the exposed Kapton inside the hole and therefore less time is needed to reach an equilibrium state again.
The effect of water is slightly different. The water molecules are absorbed by the Kapton foil. Therefore the humidity of the foil in the region which is exposed inside the hole increases and hence the dielectric constant changes[34]. The absorption of water leads to a higher charge conductivity[40] in this region and thus less charge accumulated on the surface of the dielectric, since the charges are conducted towards the copper layers where they disperse and the conductivity is very high. This means less charge is accumulated inside the hole and therefore less time is needed to charge the foil. Due to the change of the dielectric constant of the Kapton with changing humidity, the electric field inside the holes also changes, since they are closest to the region of different dielectric constant. This means a varying water content of the working gas results in a varying gain. If the water content is high enough an equilibrium (saturation) state is reached and the effect on the gain gets less. However, there are big differences in the effect of water depending on where the foils were produced (as shown in [38]). Further studies on this topic for the case of a quadruple GEM stack in the configuration intended for the ALICE TPC upgrade will be addressed in this thesis.
The above mentioned parameters lead to a gain changing with time, until an equilibrium state is reached. In addition, fluctuations in the water content may also result in a changing gain after the charging-up has finished if the Kapton inside is not fully saturated due to very low water content of the working gas. Besides this behavior, there are other factors, that affect the gain after the foil is fully charged up, for example the working gas density. Represented by T/p, temperature divided by pressure, the gain can be plotted versus the density. This can then be fitted either by a simple exponential equation or even simpler by a linear function since the variations in T/p in laboratory conditions are very small and the exponential can be approximated as a linear function. Therefore the dependence of the first Townsend coefficient on T/p can be approximated by the equations mentioned before and the gain can therefore be corrected for T/p fluctuations.
For the measurement of $\frac{\mathrm{d}E}{\mathrm{d}x}$ it is indispensable to have a well known and stable gain. Therefore, the water content has to be controlled and changes have to be noted for correction. Also, a correction for changes in the gas density has to be applied, to provide the before mentioned precise knowledge of the gain.

Of course, there are more factors that have influence on the gain and moreover on the whole behavior and functionality of the GEM, like aging effects, discharge probabilities or gas composition. Since this thesis will address only charging-up effects and dependencies of the charging-up time on ambient parameters, the latter factors are only mentioned and not explained in detail.
Before a GEM foil can be mounted in a detector, it has to been made sure that it works properly and exhibits no short circuits. To do so, high voltage will be applied directly to the foil, in contrary to the case when it is used in a detector, where it is protected

[14] in order to avoid mixing up with discharges inside the GEM (sparks), the term *cool down* will be used to express the charging down of a GEM

by resistances. The voltage applied is in the order of 500 V to 600 V depending on the environment, which means if it is done under nitrogen atmosphere or in air. Impurities on the foil, like dust or other small particles that can settle on or in the holes, might cause discharges, visible as sparks. To keep these impurities as low as possible, work with GEM foils outside a detector are done in a clean room. Figure 10 shows a $10 \times 10\,\mathrm{cm}^2$ GEM foil which is tested and cleaned by applying high voltage directly.

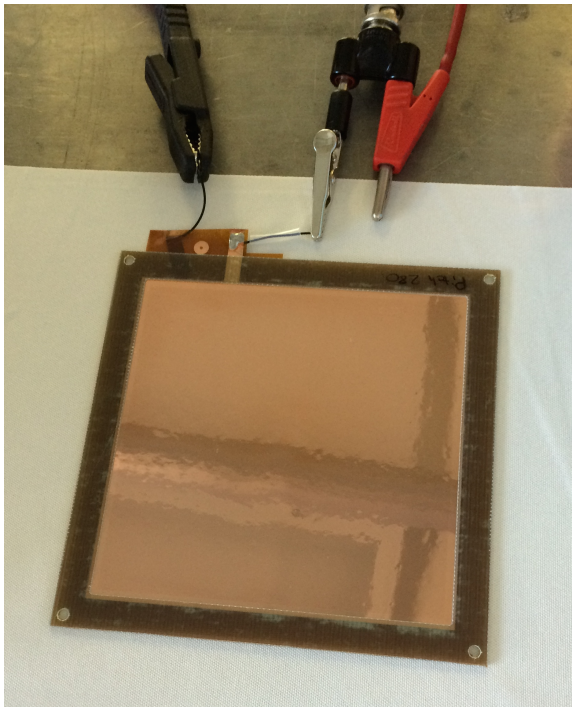

Figure 10: Testing and cleaning of a $10 \times 10\,\mathrm{cm}^2$ GEM foil in the clean room after changing the configuration of the detector; note that the red cable on the right is simply for grounding of the SHV connector above.

The testing for the foils which will be used in the ALICE TPC is similar, but more thorough and contains more steps. As soon as the foils are tested and declared to be good, they can be assembled in the readout chambers of the ALICE TPC which will be explained in the next section.

3.2. The ALICE TPC upgrade

In the ALICE TPC upgrade, planned in 2018, the whole readout will be replaced with GEM readout chambers. It will be made out of a stack of four GEM foils placed above a readout anode (pad plane) which both are glued on a strong back plate made of fiber-glass [24]. This stack will then be placed in an aluminum body. The dimensions of one full sector of the readout are given in figure 11a. A fully assembled sector is further shown in figure 11b, which means figure 11 shows both, the schematic as well as the first fully implemented prototype of a full sector. The foils are made in a so called single-mask process, which allows to make large foils in the order of 1 m. The more common small foils are usually produced in a double-mask process. The segmentation into four smaller foils, as can be seen in the schematic, is done for ease of handling during the assembly process. Therefore

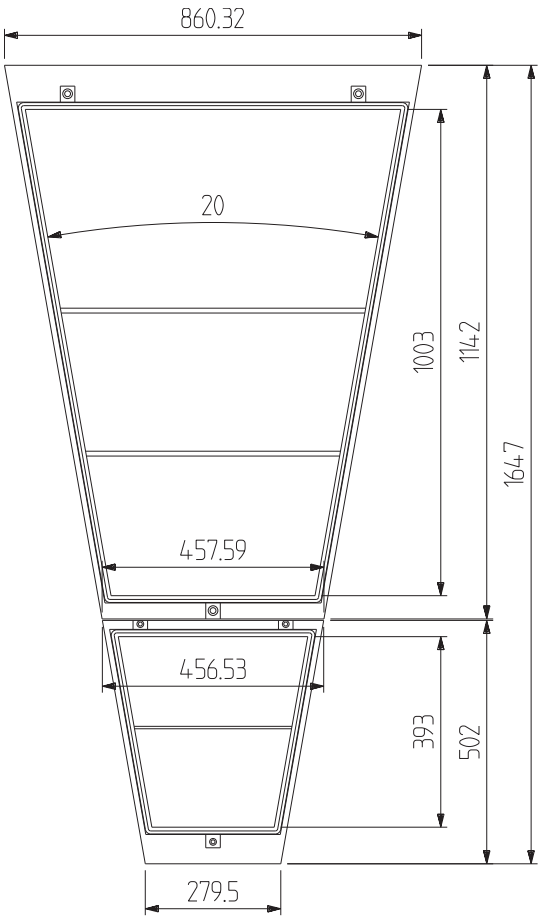

(a) Sketch of one sector from the ALICE TPC readout; dimensions in mm; adapted from [24].

(b) OROC and IROC GEM foils of one sector; courtesy of the ALICE TPC Collaboration.

Figure 11: One readout sector of the ALICE TPC, draft and first prototype.

the OROC comprises of three separate foils and the IROC of another one, which are all put together to one single readout chamber.

Further, another aspect that has to be taken into account is the capacitance of the foils. As can be seen in equation 3, the capacitance of a plate capacitor, as which a GEM foil can be approximated, is directly proportional to the area of the plates, in this case the foils. Also, the charge stored on the plates of a plate capacitor is given by $Q = C \cdot U$ and is, hence, directly proportional to the area as well. In case of a discharge inside the foil or between foils, all the charge stored on the two copper electrodes of the GEM will contribute to the discharge. This means, the larger the foils, the stronger, and therefore the more dangerous for the foil, the discharges are. To minimize the negative effects a discharge can have on the foils, one copper electrode is segmented into sectors of the same size. Figure 12 shows the segmentation for IROC and OROC foils. For example, the IROC foil is segmented into 18 sectors of about $100\,\mathrm{cm}^2$ with 2 mm distance between them. Due to this segmentation, the spatial resolution will decrease, since each gap between two sectors on the foil is like a black spot and not sensible for incoming electrons.

The gas choice for the ALICE TPC is Ne- CO_2- N_2 (90-10-5). Neon was chosen because

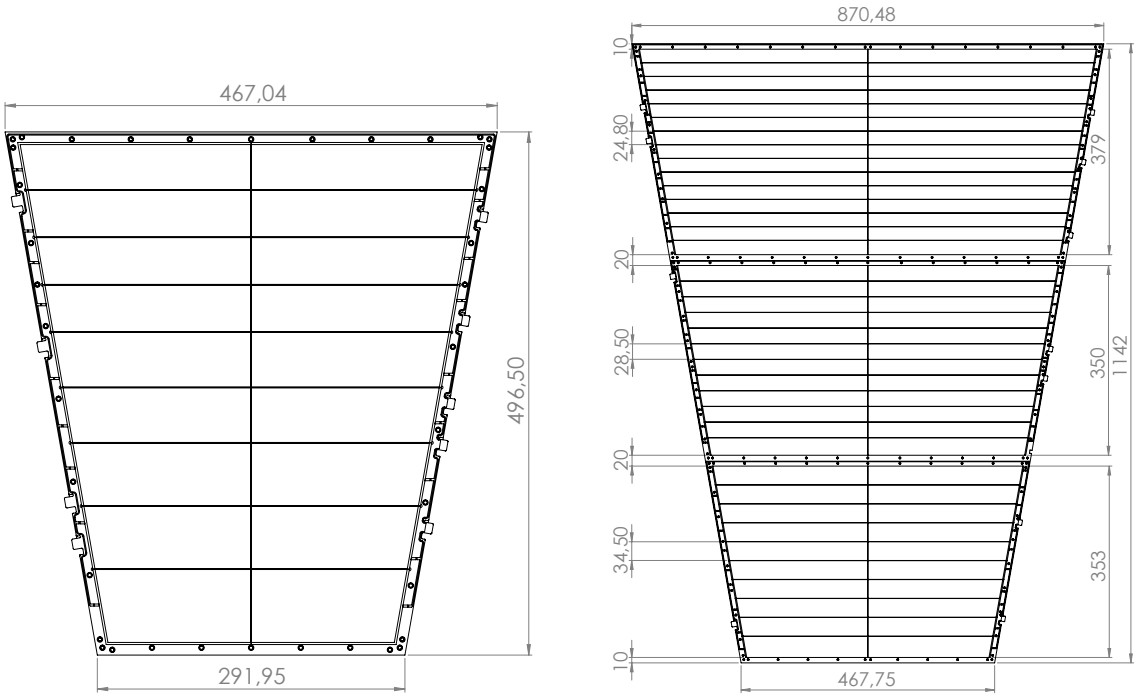

Figure 12: IROC (left) and OROC (right) foils with segmentation on one side to reduce the available amount of charge for discharges, taken from [24].

the ion mobility is higher than for argon, which has a similar performance but is cheaper. The higher ion mobility reduces space-charge effects within the drift volume and therefore leads to a more stable electric field. Nitrogen as an additional quencher gas helps to prevent avalanche multiplication between the GEM foils and thus provides a more stable operation of the readout chambers. The combination of CO_2 and N_2 as quencher gas in the given composition also brings the advantage of a moderate decrease of the drift velocity compared to the necessary positive effects.

To power the GEM stacks 144 HV channels are needed, 72 for each side of the TPC. These HV channels have to provide 6 kV. For one sector, four channels are necessary. One channel for the IROC and three synchronously operated channels for the OROC. Even though a complete OROC could be powered by one single channel, three are used to provide more flexibility and stability. In addition to these 144 HV channel, the same number is needed to set the voltage on the cover electrode, which has to match the last strip of the field cage. The distribution of the channels is the same as above. Further features the power supplies have to ensure is remote controllability, current resolution $\mathcal{O}$(nA) and fast trip mechanisms for safety of the foils [24].

Once all dependencies between the gain and ambient parameters like pressure and temperature are fully understood and quantified, the gain can be corrected offline to obtain a stable value of 2000 for $\frac{\mathrm{d}E}{\mathrm{d}x}$ measurements. This stability is necessary, since the energy loss is proportional to the number of electrons arriving at the readout pads. This knowledge allows not only to reconstruct the track of a particle but also identify it from its mean energy loss.

3.3. R&D for ALICE

The R&D for the ALICE TPC takes place on different scales. On the one hand, there are small detectors used in the lab to do research on the behavior of GEMs and to find the optimal working parameters for example. Further the aging of GEMs and the rate capability is studied. On the other hand, prototypes of OROCs and IROCs are built to learn how to assemble them and how to test them to assure the quality. Also, studies were done with an IROC in the CERN PS to determine the performance under realistic condition and to measure the $\frac{\mathrm{d}E}{\mathrm{d}x}$ resolution.
The latter is done by using beams of specified particles with defined momentum, for example 1 GeV pions and electrons. This beam is produced in fixed target collisions with a test beam taken from the CERN PS. Depending on the target a secondary beam of a certain kind of particles can be produced, with a small admixture of other types as well, and then be directed through a gas volume where it ionized the gas and the track is read out by the IROC, or OROC respectively, prototype. The goal of these tests is to provide full operational capability, no dead spots on the read out and gain uniformity of the chamber. Also the gain can be equalized if it does not show the same value along one track, since the particle and its momentum are well known, which means the signal on each readout pad should be the same. Another quantity that can be determined in such tests is the energy loss resolution. This is done by analyzing each track for the total energy loss of the particle that has produced it. Since all all particles are the same and have the same known momentum, it is possible to plot the number of measured energy losses. This leads to a Gaussian like distribution from which the mean $\left\langle \frac{\mathrm{d}E}{\mathrm{d}x} \right\rangle$ and the width $\sigma\left(\frac{\mathrm{d}E}{\mathrm{d}x}\right)$ can be determined. The ratio between these two quantities then gives the $\frac{\mathrm{d}E}{\mathrm{d}x}$-resolution. Tests with first prototypes in the CERN PS testbeam show resolutions of 10 to 12%.

4. Measurements

The experiment was performed at *CERN*, Geneva. The setup with the quadruple GEM detector was already there and finished, only a few changes had to been made. A detailed view on the detector is given in section 4.1.1.
To power the detector, remotely controllable power supplies were used. Therefore a program, implemented in *LabVIEW*™, to control and read them, was used. A functioning version of this program was also already there, but modifications were needed. The changes in the program are listed in section 4.1.2 including the ways they were implemented.
Since the GEM foils are very fragile and easy to destroy it was important to get used to the setup and the behavior of the detector itself in a more safe way. Hence, the first trials on how to ramp the voltages up and down and getting used to the program have been done without detector. Once being familiar with all the functions and buttons, the detector was connected to the high voltage supply. The first measurements have been performed with Ar-CO_2 (70-30) as the working gas, for which the results are shown in section 4.2.
During my measurements with Ar-CO_2 the first prototype of an active voltage divider (AVD) [41] was finished. In section 4.3 the first commissioning of this device is shown.
After the setup has been fully understood, the gas mixture has been changed to Ne-CO_2-N_2 (90-10-5), the expensive working gas of the ALICE TPC. The results of these measurements are presented in section 4.4. After the comparability between Ne-CO_2-N_2 and Ar-CO_2 has been ascertained, the gas mixture has been changed back to the cheaper Ar-CO_2. The results will be shown in section 4.6.

4.1. Experimental Setup

The experimental setup can be divided into three parts: the box, the power supplies and the computer; see figure 13 and figures 35, 36 and 37 in the appendix.

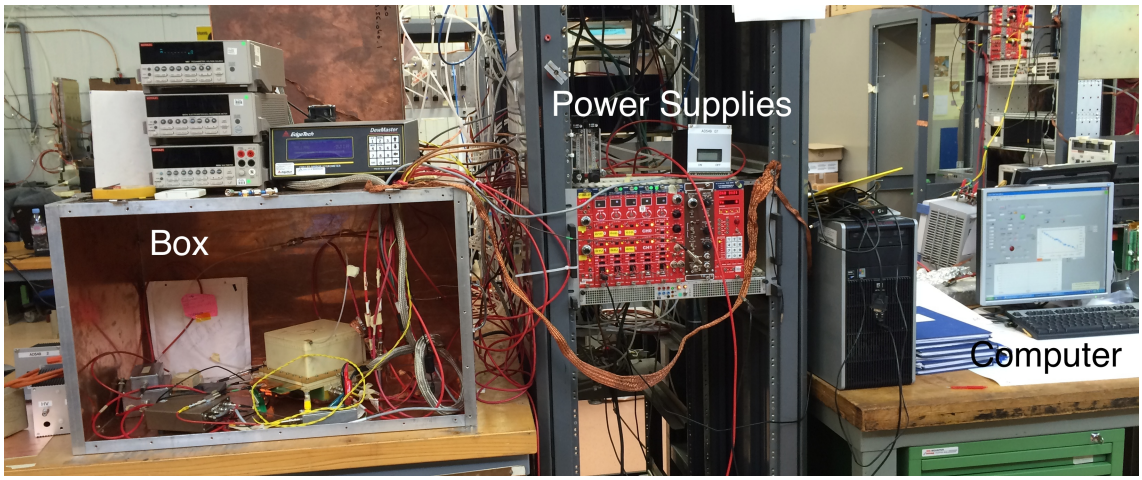

Figure 13: Experimental setup; copper box with detector inside and picoammeter and water sensor on top (left), power supplies (middle), computer for control and readout (right).

The copper box contains the detector, the temperature and pressure sensor with an analog input for the water-sensor - on top of the box - to measure the water content of the gas

and a protection circuit for the picoammeter. All the necessary cables and the gas supply lines come in through a hole on the top of the box.
The high voltage power supplies for the GEMs are set to negative polarity and have a maximal voltage output of about 8000 V and a maximum current output of 300 μA. They have two channels and they are remotely controllable via USB connection. The power supply for the drift field has four channels and an power output of about 8000 V, too, but a maximal current of 3 mA[15]. It is also remotely controllable. Above the power supplies, there is a flow meter which controls the amount of gas through the detector.
The computer is connected to all measurement devices for control and readout. The *LabVIEW™* program then reads all the devices and saves the acquired data to file.
The gas supply consists of mixer and remotely controlled flowmeters to adjust the flow for the different gases and thus the compound of the working gas. For the Ar- CO_2 (70-30) measurements premixed gas was used, for which the mixer was bypassed and the flow was controlled with a manual flowmeter (visible in figure 36). The measurements with the Ne- CO_2- N_2 (90-10-5) were done using premixed Ne- CO_2 (90-10) and adding 5% of nitrogen in the mixer.
The gas supply lines are made of stainless steel and copper to reduce water enrichment of the gas as much as possible. On the top side of the detector box, there is an inlet for the gas and on the bottom of the box there is an outlet which is connected to the water sensor to analyze the water content of the gas.

4.1.1. Description of detector prototype

The detector used in the experiment is a quadruple GEM detector, consisting of a plate on which the pad plane and the GEM stack is placed and a chassis which contains the field cage and seals the volume gas tight.
A schematic of a quadruple GEM detector is shown in figure 14. As indicated by its name, the detector is made of a stack of four GEM foils mounted above a readout anode (pad plane, also see figure 38). A picture of the inner part of the detector is shown in figure 39 in the appendix. Originally, the configuration of the GEM stack has been *SP-S-LP-S*, which is **S**mall **P**itch - **S**tandard - **L**arge **P**itch - **S**tandard[16] from the top GEM to the bottom GEM. The changes that have been made, are replacing the *SP* with a *LP* foil and interconvert foil 1 and 2. After the last foil died during measurements and since there was no standard foil available, it has been replaced by a medium pitch foil (Medium Pitch: 200 μm). Hence, the new configuration of the foils is *S-LP-LP-MP*.
The first measurements have been done with an induction gap of 3 mm. However, since the AVD was designed according to parameters from the ALICE TPC TDR, the induction gap was adjusted to 2 mm for better comparisons between AVD and the setup with multiple power supplies and of course to match the planned settings for the new ALICE TPC readout.
The field cage inside the chassis is shown in figure 15. It is made of a chain of nine 10 MΩ

[15] 3 mA for 0 - 2000 V, 2 mA for 2000 - 4000 V, 1 mA for 4000 - 8000 V
[16] Standard: 140 μm; Large Pitch: 280 μm; Small Pitch: 80 μm [24]

resistors and a tenth (not visible in the figure) 121 MΩ resistor to ground to match the voltage on the first foil. The resistor chain is used to achieve a potential gradient and is powered with a separate HV channel because current is necessary for the voltage division but unwanted in the drift cathode. That way, the voltages on the strips decrease (absolute) from the drift cathode downwards and the field, thus, becomes homogeneous (see section 2.1). One can also see the drift cathode with holes in it for the radiation. The reason for the holes is to minimize the radiation length of the chassis. However, to provide gas tightness the holes need to be covered, for which a very thin polymer (Mylar) layer is used. The HV connection for the drift cathode is visible in figure 15 on the top left side; also the HV connection for the first strip of the field cage is visible slightly right to it.

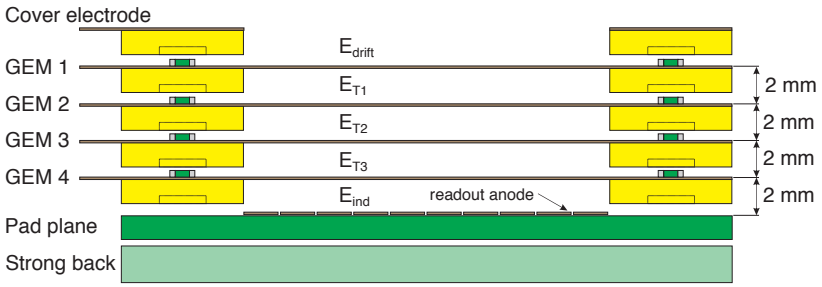

Figure 14: Schematic of quadruple GEM stack without drift cathode and field cage; shown are the support frames (yellow), the pad plane (green), the foils (black), the gaps between the foils and the fields; adapted from [24].

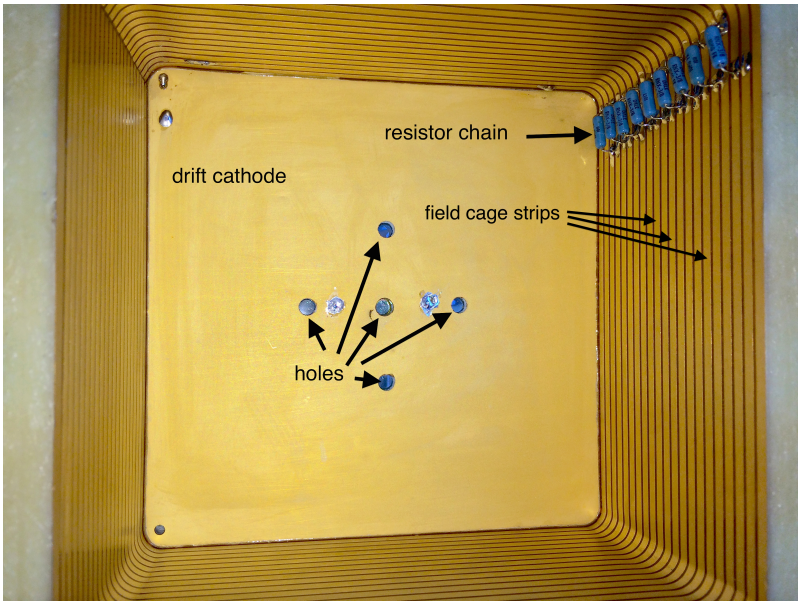

Figure 15: Look inside the chassis with the field cage; resistor chain, drift cathode and holes for radiation are visible.

The HV supply for the GEM foils comes from SHV connectors placed on both sides under the pad plane. For GEM4 bottom an additional external 15 MΩ resistor to ground is connected. The reason for this resistor is as follows: the polarity of the power supply is negative, which means there is no electron flow towards the power supply. In GEM4, there are the most electrons, since the gas amplification starts in GEM1 and therefore the

primary electrons have been amplified in three GEMs before they reach the last one. Since some electron accumulate on the bottom of each GEM, it is necessary to carry them away. This is only possible if they can flow towards ground potential because of the negative polarity of the power supply.

4.1.2. HV and readout

LabVIEW™ is a graphical programming software from *National Instruments* that allows to create custom made programs to control devices for experiments, read out data and plot the data live. In the existing program one could enter the voltages across the GEMs and the transfer fields, click the *Set*-Button and the program set the entered values in the power supplies. The communication between the LabVIEW™ and the power supplies is done through the RS-232 protocol, which is a serial communication. Further one could change the ramping speeds, maximum voltages and currents, as well as the detector parameters such as drift distance, resistors or gaps between the GEMs. It also displayed the live plots of the voltages across the GEMs and the transfer fields.
In the ideal case the power supplies ramp the voltages synchronously, but due to the serial communication, the commands to ramp the voltages are given one after another and also in a random order. To protect the foils from peak voltages which result from this random ramping order[17], a specific ramping order has been implemented: ramping up (*Go Ready*) GEM4d → GEM4u → GEM3d → GEM3u → GEM2d → GEM2u → GEM1d → GEM1u → Drift;
ramping down (*Go Safe*) is just vice versa, except for the drift voltage which is left as it is. Figure 16 shows the implementation.

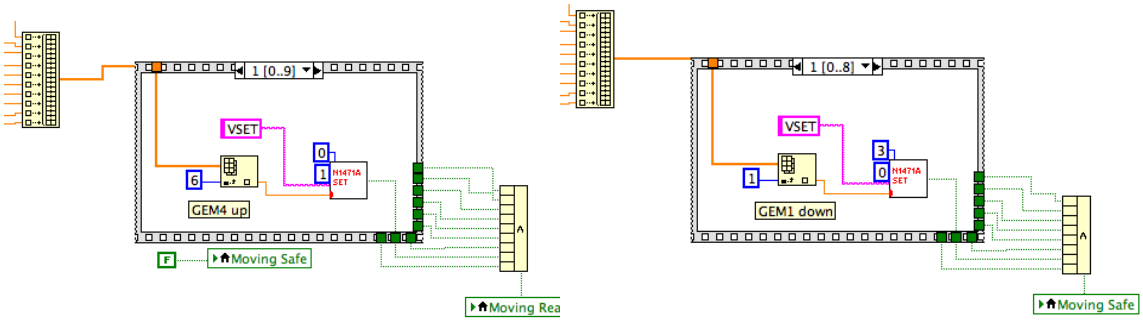

(a) Implementation of the ramping up part of the program; command string to power supply (pink) and value to set to (blue case, bottom left).

(b) Implementation of the ramping down part of the program.

Figure 16: Implementations of the ramping orders.

The two modes, *Safe* and *Ready*, refer to whether the detector operates with or without amplification. This means, in *Safe*-mode the voltages are ramped down to a point where no amplification occurs anymore. In *Ready*-mode the voltages are set to their nominal values.

[17] e.g. VG1d starts ramping down first and VG1u starts last, depending on the ramping speed this might result in a difference of several tens of volts which could cause discharges in the worst case

Further, a feature to just click one button and the power supplies were set to the nominal voltages has been implemented. Also to go to safe mode one single button has been added. For *Safe* it is now possible to choose the nominal safe voltage for GEM1, plus, define a percentage of the nominal voltages which represent *Safe*-mode.
Another issue with the existing program was the data extraction. It was possible to write the measured data to a file, but if the program crashed for example, all data was lost before it was saved. Therefore the data saving feature has been changed as well. It now includes a number of new features: naming the spreadsheet according to date and time the program was started, saving the data every time a certain number of measurements is reached and thus prevent data loss in case of a unforeseen crash of the program, enabling of easy exportation for analyzing and the addition of new sensors. The implementation is shown in figure 17.

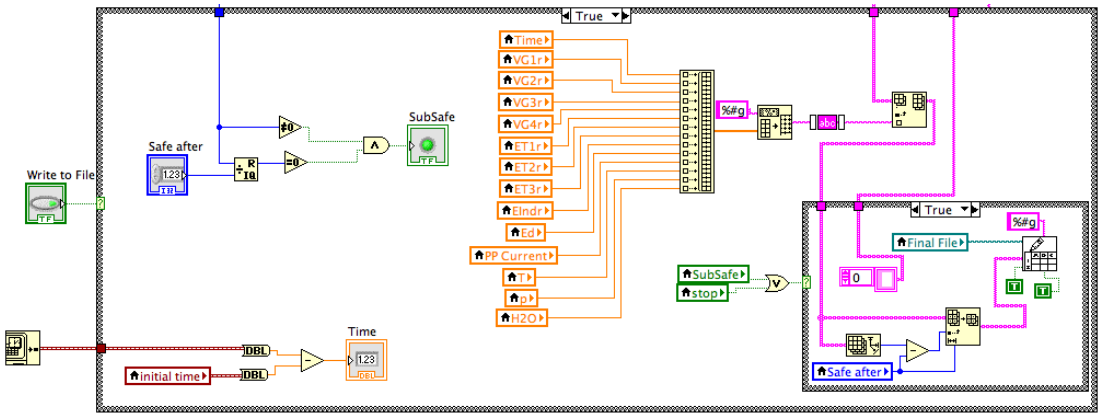

Figure 17: Implementation of the saving to file part.

The new sensors that have been installed are: *MSR® 145* for measuring the pressure and the temperature of the surrounding air and the water content of the gas via an analog input; *Edge Tech® Dew Master* which is connected to the analog input of the former sensor; *Keithley® 6487* for reading the current on the pad plane which is proportional to the gain.

4.2. First measurements with Ar-CO_2 (70-30)

The first measurements to understand the overall behavior of the detector and to finalize the setup have been done using Ar-CO_2 (70-30) gas mixture. The gas was premixed and also used by other experiments in the laboratory, however, each one with its own supply line, but all connected to the same central line to the gas bottle. Between the pad plane and the picoammeter a protection circuit was connected, which consists of diodes and resistors to protect the Keithley from high discharge currents. During these measurements, it became apparent that this kind of protection circuit distorts the results quite a lot and makes it therefore less meaningful. Also, a grounding problem for the picoammeter, which distorted the measurements,too, has been found. Still, I will use this data to show the effect of this protection circuit compared to a single serial resistor, the effect of the proper grounding (both see section 4.4) and to explain the fit equation and the ideas behind the

Table 3: Nominal voltages for Ar-CO_2 (70-30) and Ne-CO_2-N_2 (90-10-5); values for the argon mixture result from increasing the values for the neon mixture step by step until the current on the pad plane was in the order of nA; new settings for argon result from measurements with neon and the settings according to the ALICE TPC TDR which yield a gain of 2000.

	Ar-CO_2	**Ar-CO_2** (new)	**Ne-CO_2-N_2**
E_{drift} (V/cm)	400	400	400
ΔGEM1 (V)	350	325	275
ΔGEM2 (V)	315	283	240
ΔGEM3 (V)	329	300	254
ΔGEM4 (V)	392	375	317
E_{T_1} (kV/cm)	2	2	2
E_{T_2} (kV/cm)	3	3	3
E_{T_3} (kV/cm)	1	1	1
E_{ind} (kV/cm)	4	4	4

measurements.

To take data, a ^{55}Fe source has been placed on top of the detector box, such that the opening of the sealed container aligns with one of the holes on top of the box. ^{55}Fe decays with a half-life of $t_{1/2} = 2.744\,\text{a}$ under the emission of X-ray photons at a energy of $E = 5.9\,\text{keV}$[42]. The initial activity of the source was $A = 1.11\,\text{GBq}$ on 01/09/2012, which means the current activity is roughly 550 MBq.

Then the HV has been ramped manually[18] to the safe settings, which in this case have been the nominal voltages, except for the voltage across the first GEM, which is set to 0. The ramp speeds have been set to 10 V/s for both, up and down. The nominal voltages for the argon gas mixture are higher than for neon. Both are shown in table 3. After the replacement of the protection circuit, the voltages changed again, since the current measured on the pad plane was way to high. Further settings for the power supplies have been: 5500 V (8100 V for the drift cathode, respectively) maximum voltage, 100 μA current limit for the field cage and 0.5 s for the trip, which means if current limit is exceeded for more than 0.5 s the power supply gives out an alarm and the program initiates the ramp down. The current limits for the particular channels which power the GEM foils were set to 5 to 10 μA , except for the bottom side of the last foil, for which it was set to 200 μA since it has a 15 MΩ resistor to GND connected.

After all voltages are set, the picoammeter is read out and the voltage across the first GEM is ramped up to its nominal voltage. On the on-line plot in the LabVIEW™ program the current on the pad plane, measured with the picoammeter, becomes visible. At the beginning of the ramp the current does not change at all. Just as the voltage across GEM1 reaches a certain value the gas amplification sets in, the current on the pad plane increases and the plot shows a spike. The value the picoammeter measures has a negative sign because it measures electrons, and hence negative polarity.

[18] thus it is possible to react immediately if something does not go as planed, e.g. I hear discharges from inside the box, and there is no need to do this fast

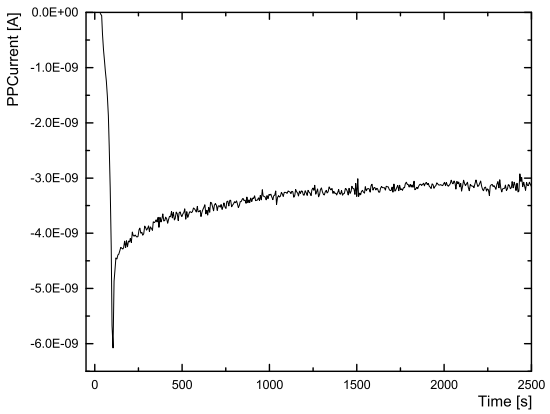

(a) Ramping up of the voltage across GEM1; one can see a steep increase of the current at the very beginning of the measurement (left); after the increase one can see a slow but steady decrease; note the negative polarity and therefore the current increases absolutely when going downwards.

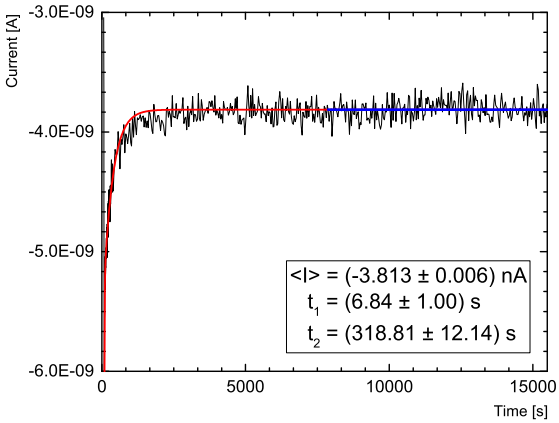

(b) Sum of two exponentials as fit function to find time constant after ramp up.

Figure 18: Ramps with ^{55}Fe.

Figure 18 shows two measurements, for which the current on the pad plane is plotted versus the time. In figure 18a one can see about 40 minutes of measurement. The actual ramp lasts only about 35 seconds, visible on the left side of the plot as a very steep increase of the current. After the ramp is finished the current decreases in an exponential shape. In figure 18b this decrease is fitted with a sum of two exponential decay functions:

$$I(t) = I_0 - A_1 \exp\left(-\left(\frac{t-t_0}{\tau_1}\right)\right) - A_2 \exp\left(-\left(\frac{t-t_0}{\tau_2}\right)\right) \tag{5}$$

The parameter I_0 is fixed and determined by averaging the rather steady region of the current, visible as a blue line representing a linear fit with slope 0. t_0 is the time offset, since the maximum current is reached after the ramp is finished, which, however, takes some time as mentioned before. The fit gives two time constants τ_1 and τ_2 after which the current decreases to $1 - \frac{1}{e}$, $\frac{1}{2e}$ respectively, of the steady current. The meaning of the two time constants can be explained as follows. The idea behind all these measurements - and this thesis overall - is to find out how charging-up effects affect the gain and how long it takes until the whole system is charged up. Therefore, one can divide the system into two parts, namely the HV supply and the detector itself. When ramping up the voltage, the cables charge up due to their capacitive character. In addition to that, the detector itself comprises some capacitances. Each foil and the drift cathode represent a capacitor that charges up as soon as a voltage is applied. These charging-up processes define the first time constant τ_1. The second time constant, τ_2, is determined by charging-up effects inside the GEM foils, as explained in section 3.1.

As can be seen in figure 18b the current on the pad plane shows statistical fluctuations

around a mean value. This is due to the statistical characteristics of radioactive decay. In addition, the current exhibits some less frequent and longer lasting changes which are assumed to result from changes in the gas density, but, as will be shown later, also due to the protection circuit. The effect of the gas density on the gain is a known effect and can be corrected. This correction will be explained in section 4.5 with data taken after the replacement of the protection circuit and the assuring proper grounding.

The next measurements have been done using a ^{90}Sr source. ^{90}Sr decays under the emission of electrons with $E_{max} = 545.9\,\text{keV}$ to ^{90}Y, which means it is a β^- decay. The subscript max is used, since the β decay shows no line spectrum which is due to the neutrino as a third particle. Therefore the energy of each particle is not fixed due to the conservation of momentum. Its half-life is $t_{1/2} = 28.8\,\text{a}$ [42]. Further the Yttrium nuclei decay with a half-life of $t_{1/2} = 2.67\,\text{d}$, also under the emission of electrons of energy $E_{max} = 2279.8\,\text{keV}$, to zirconium. This means, compared to ^{55}Fe X-rays, the electrons from the strontium source produce a lot more ionization electrons in the gas. Therefore, the activity of the ^{90}Sr source can be much lower but still show the same current on the pad plane at the same gain of the detector. The activity of the strontium source used for the measurements was $A = 3\,\text{MBq}$ on 01/05/2005 and therefore it is now about 2.4 MBq.
The measurements have been performed in the same way as with the iron source.

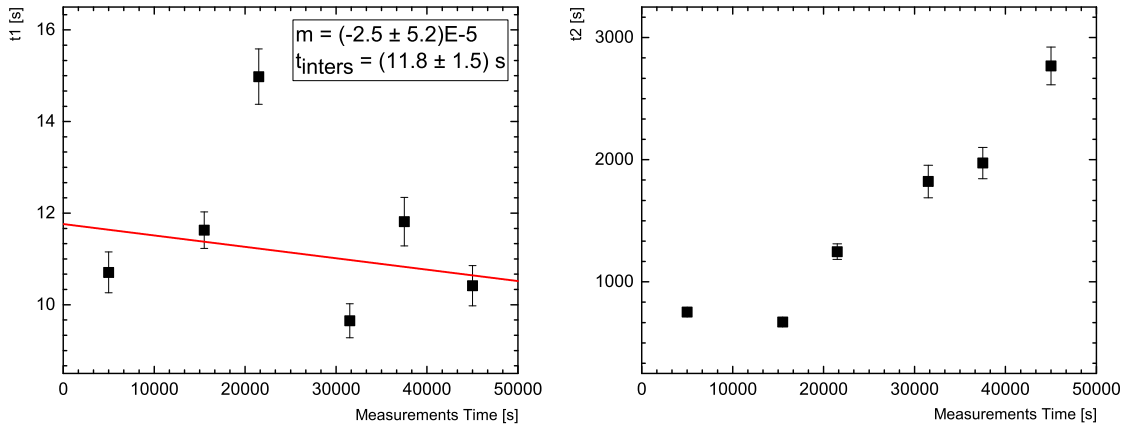

(a) Time constant τ_1 plotted versus the measured time.

(b) Time constant τ_2 plotted versus the measured time.

Figure 19: Dependence of the time constants τ_1, τ_2 on the measured time t.

The thereby acquired time constants have been plotted versus the overall measured time, as shown in 19. As expected, the values for τ_1 are almost the same for different measurement time, since the respective parameters like cable length for example do not change. The plot is shown in figure 19a. A linear fit even shows a very slight decrease of $25\,\frac{\mu\text{s}}{\text{s}}$. Even for very long measurement times of several tens of thousands of seconds, this only leads to less than a second change in τ_1 which is negligible. Figure 19b shows the same plot for τ_2. The difference between the two plots is obvious: τ_2 increases almost linearly with time. To a certain extent this is an artifact resulting from the fit function, which is

an exponential and therefore asymptotic. Nevertheless, the current should at some point stabilize to a constant value - with random fluctuations - and thus the time constant should also have a maximum value. It is assumed that this is an artifact of the protection circuit and due to additional charging-up of the diodes and their leakage current.
Still, to make sure for successive measurements, that this steady increase with the duration of the measurement is no artifact of the fit procedure - where the exponentials show asymptotic behavior - one longterm measurement has been chosen and fitted for different time intervals. The fit starts always at the maximum of the current and is done up to a certain time. Just like before, the offset I_0 is determined by averaging the current. For the region where the current is not steady, yet, an interval of 5000 s around the end of the fit is averaged. As soon as the the end of the fit lies in the steady region, the mean of the current in the steady region is averaged up to the end of the fit. An example is shown in figure 20a.

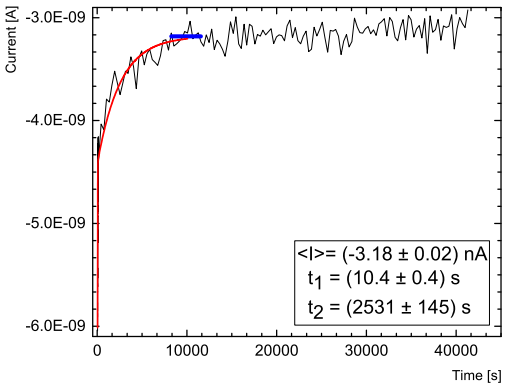

(a) Example of fitting an interval; red line is the fit, the blue line is to determine I_0 as an average around the end of the interval.

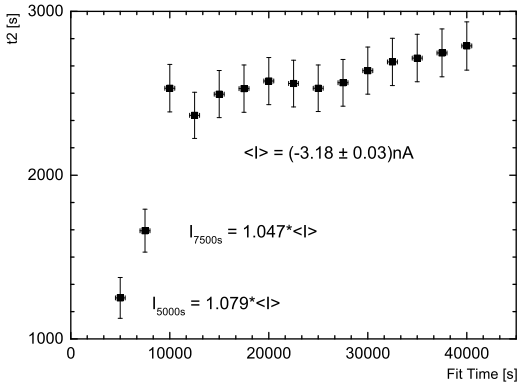

(b) Time constant τ_2 versus the time interval which was used for the fit.

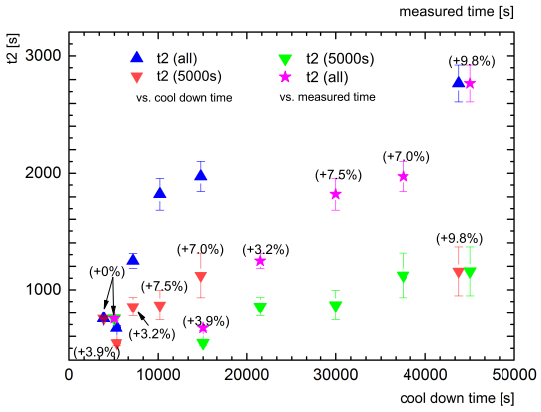

(c) Time constant τ_2 versus cool down time and measured time.

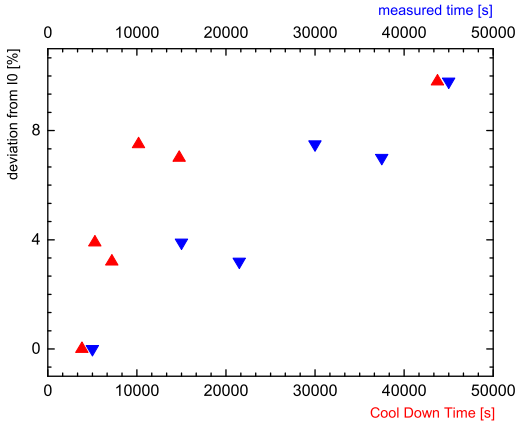

(d) Relative change of the offset current I_0 for different fit intervals versus measured time and cool down time.

Figure 20: Explanation of fit procedure and results of the dependence of the measured time and the time constant τ_2 as well as the dependence on the cool down time.

The result of this analysis is presented in figure 20b. One can see, that the time constant τ_2 increases towards longer fit intervals and reaches a plateau at about 10000 s. For very long fit intervals τ_2 increases again slowly, which can be explained with the steadily increasing current with time and therefore an increasing mean value for larger averaging intervals. In addition, it is to mention, that for fit intervals smaller than 10000 s the time constant τ_2 is less than half the value of the plateau, however, the current offset for these intervals is up to 8% greater than for the plateau region. In figure 20b the current offset of the plateau region is denoted with $\langle I \rangle$. The observed results show that the fit interval has no effect on the time constant and therefore it should also be independent on the duration of the measurement, as long as the measured time exceeds the charging up time.
Another factor that might affect the charging-up time is, as mentioned in section 3.1, the cool down time of the detector, which means the time the detector has been in at no gain settings before the measurement starts. Figure 20c shows the time constants τ_2 versus the cool down time for six different measurements (blue and red). Since these measurements show the same increase as the ones before, but are expected to have a plateau at some point where the foils are fully discharged, they were repeated without protection circuit and with proper grounding. The results will be presented in section 4.5. Only in case all fits end at $t = 5000$ s a plateau starting at 37000 s for τ_2 can be interpreted. But, the value for the time constant obtained from this measurement is for a mean current of 9.8% more than the overall average of the steady region.
Figure 20d additionally shows the trend of the relative deviation of the offset current for the fits in the interval up to 5000 s to the mean current offset for the fits over the whole measured time. Again the results are shown for both times, the measured time, blue, and the cool down time, red. Once again, there is no obvious plateau visible and the deviations reach up to 10% for the measurements that have been done.
For later measurements the fit function can be transferred, since the idea behind it will not change by replacing the protection circuit. Also it can be focused on the cool down times, since the dependence on measured time is ruled out.

After these measurements were done, the first prototype of an Active Voltage Divider[19] for a quadruple GEM stack was commissioned and tested. This is presented in the following section. Then a few measurements using the Ar-CO_2 (70-30) mixture were done, to prove the proper function of the device. During these measurements the protection circuit was replaced by a simple 100 kΩ serial resistor. Along with the replacement of the protection circuit the gas mixture has been changed to Ne-CO_2-N_2 (90-10-5). The repeated measurements for the dependence of τ_2 and the cool down time are presented in section 4.5.

4.3. First Commissioning of a Active Voltage Divider for GEMs

One major disadvantage of the previous used setup with multiple power supplies is the issue with synchronous ramping. This can be remedied by using a voltage divider, which is in its

[19] designed and built by H. Müller, CERN

Table 4: Nominal voltage setting according to ALICE TPC TDR[24] and voltage output of AVD; set voltages as well as measured.

	nominal	**calculated**	**measured**
GEM1 (V)	275	267.7	284.9
GEM2 (V)	240	241.4	245.5
GEM3 (V)	254	248.5	254.3
GEM4 (V)	317	316.6	323.1
E_{T_1} (kV/cm)	2	2.040	2.13
E_{T_2} (kV/cm)	3	2.985	3.00
E_{T_3} (kV/cm)	1	0.996	0.98
E_{ind} (kV/cm)	4	3.990	3.85

simplest configuration only a resistor chain. Thus, only one power supply is necessary to power the foils. These simple circuits also come with a small disadvantage, namely the load dependence of the voltage output. The active voltage divider (AVD) avoids this problem by using transistors in the dividing chain. Figure 21 shows both a schematic and picture of the AVD. Voltage in and outputs, as well as the e-fuses are indicated in the figure.
The output voltages of the AVD are shown in table 4. As one can see, the differences between the nominal voltages and the output voltages are not even and reach up to about 3%.

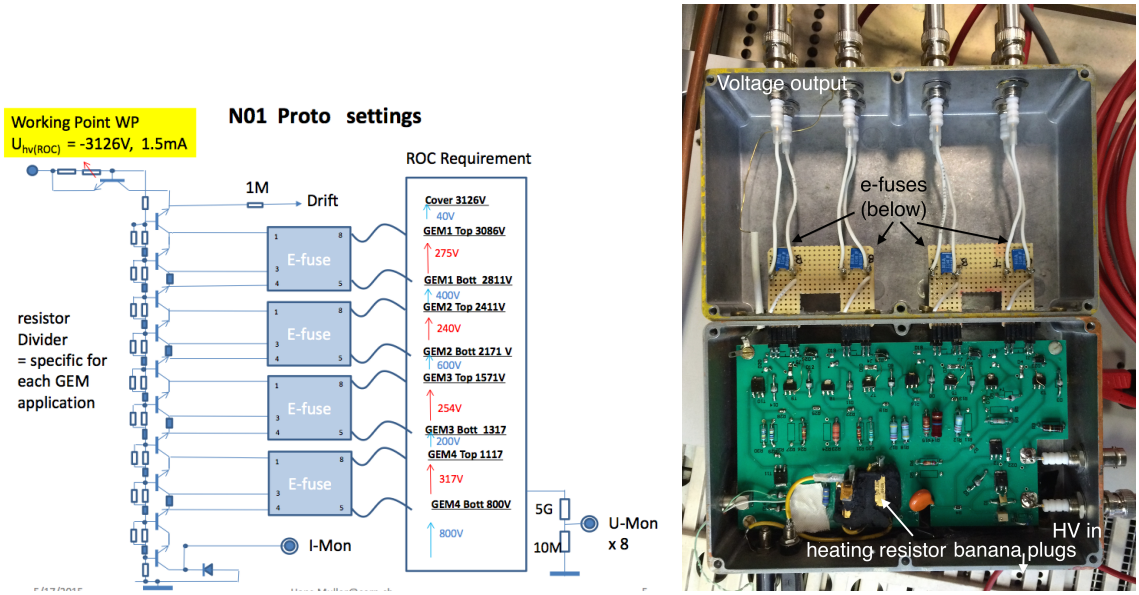

Figure 21: Circuit diagram of the AVD (from manual by H. Müller) and picture of the open prototype box showing the PCB and the e-fuse box.

Further the AVD also contains electric fuses (e-fuses) which protect the foils. In principle, the e-fuses are 50 kΩ resistors, that change their resistance drastically for currents above a certain level. That means, if the current output of the AVD for one foil is higher than 40 μA, e.g. due to a discharge, the resistance of the e-fuse increases by a factor of 130 to 6.5 MΩ and thus the voltage drop across the e-fuse increases directly proportional to the change in the resistance according to Ohm's law: $U = RI$. Therefore, the voltage across the GEM foil is reduced by this amount, leading to no amplification in the respective foil

and the prevention of further discharges. As soon as the threshold current for the e-fuse is deceeded the resistance drops back to the initial 50 kΩ and the voltage in the foil goes back to its actual value. Triggering an e-fuse does not significantly affect the potentials on other electrodes, as can be seen in figure 22. The voltage change in the GEM for which the e-fuse was not triggered is about 750 mV which is negligibly low.

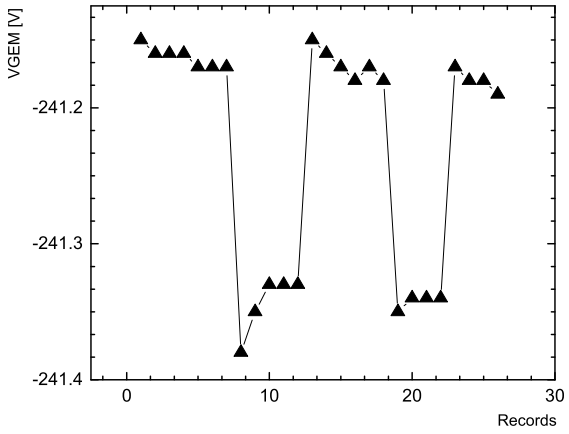

Figure 22: Effect of triggering the e-fuse for GEM2 on voltage of GEM3.

Ramping up the AVD shows for the output voltages a nonlinear behavior due to the bias of the e-fuses for input voltages smaller than 1500 V. For higher voltages the ramping behavior is linear and proportional to the input voltages, although the slopes for the different GEM voltages are not the same.
Some more features of the AVD are monitoring several parameters, like voltages and temperature. The voltage can be monitored via banana plugs on one side of the box as indicated in figure 21. They always need to be measured to GND and are a factor of $\frac{1}{1000}$[20] of the real voltage output. Depending on the multimeter a correction factor has to be multiplied with the measured value.
However, the AVD, too, has some downsides. The electronics on the PCB[21] dissipate heat, about 4 W in total. For an application in the ALICE TPC the box has to be cooled. For the first tests the only requirement is that the PCB is in a thermal equilibrium, since the resistances are a function of the temperature. The heating up of the PCB takes roughly 44 minutes and the equilibrium temperature is about 40°C. During this time, the voltages in the GEM foils change, since the current in the resistor chain changes. Hence, the amplification changes as well, which can be observed in the current on the pad plane. Respective plots will be shown in the next section. To monitor the temperature of the board, three different options have been used. The first option is to put a temperature sensor directly onto the board. For the second option is measured the current output of the power supply, since this current is equivalent to the current in the resistor chain and therefore also proportional to the temperature on the resistors and the board. The last option is to put

[20] for a 10 MΩ multimeter
[21] Printed Circuit Board

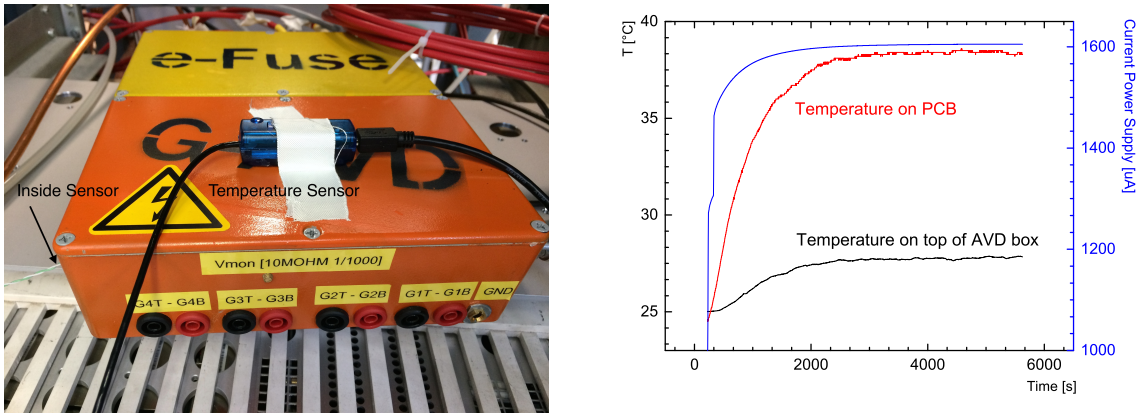

Figure 23: Setup for monitoring of temperature and comparison between the three methods.

a temperature sensor on top of the box. Figure 23 shows the setup of the temperature monitoring and the comparison between the above mentioned options.

It is very obvious from the plot, that the temperature measured on top of the box is less than on the board itself, which is simply due to the distance from the heat source, the heat capacitance of the box and the dissipation of the heat throughout the box. The shape of the plots is the similar, though. Note, that the data was taken using two different sensors to be able to take data from the same heating up process. The temperature on the board was measured with an *Agilent* Multimeter and read out with the respective software. The plots show that as soon as the equilibrium temperature is reached, both the current from the power supply and the temperature on top of the box are steady. As a consequence, it is not of necessity to measure the temperature on the board and on top of the box. For qualitative measurements the knowledge about the current from the power supply is enough to tell roughly at which time the PCB was heated up completely.
Since the heating up process takes quite long (about 44 minutes), an additional 4 Ω heating resistor - marked in figure 21 - was put onto the PCB. It is powered with about 9 V at a current of roughly 1 A. Therefore the heating power is about 3.5 W. The heating from the equilibrium temperature in safe mode, about $27°C$, to the ready temperature of about $40°C$ takes between 2 and 3 minutes. It is to mention, that only one resistor is used to heat the PCB, which means, the heat is only transferred to one area of the board and needs to dissipate from there through the rest of the board. Hence, it takes some time between the heating and the settling of a homogeneous temperature on the board. After the board is at its working point regarding the temperature, the measurements can be started.

In the next version of the AVD some changes should be made. It is planned to put more but smaller heating resistors on the board, to gain better and more uniform heating. Plus, the monitoring of the voltages shall become more accurate.

4.4. Measurements with Ne-CO_2-N_2 (90-10-5)

As mentioned in section 4.2 the protection circuit which was using diodes was replaced by a single 100 kΩ resistor in series between the pad plane and the picoammeter. The effect on the current measured was big.

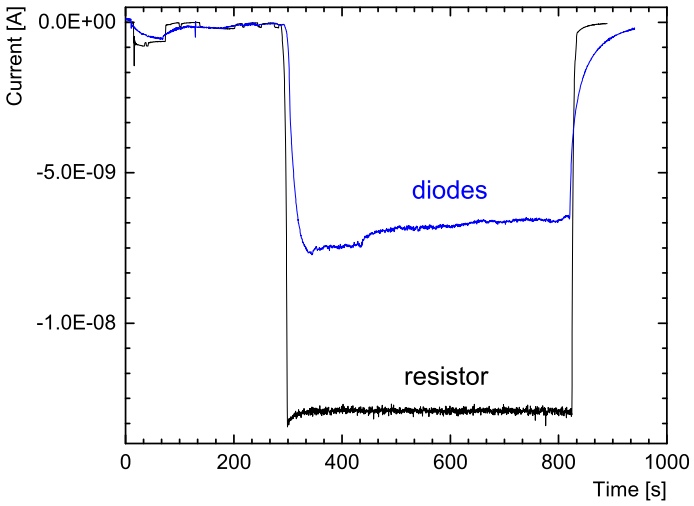

Figure 24: Comparison between the two protection circuits used for the picoammeter; ramping up from 0 to nominal for GEM1, GEM2-4 at nominal in *Safe*-mode.

As can be seen in figure 24 the current measured with the diode protection circuit is about half of that measured with the resistor only, even though the voltages have been exactly the same, which is due to their high leakage current of several nanoampere. Further the current with the resistor is much more stable and shows no steps and does not decrease with time. Another clearly visible effect of the diodes is the shape for ramping up and down. Whereas for the measurement with the resistor, the current increases almost instantly, it shows almost an exponential increase for the diodes and a step at about 410 s. The ramp down exhibits the same behavior, only vice versa. A similar shape of the curve can be observed for capacitors, which leads to the assumption, that the diodes posses relatively big capacitances, in addition to the big leakage current.
After the replacement, the AVD was connected and the voltage was ramped up to check the gain and the trend of the current. This time the current exhibited again an overshoot, which was not observed with the multiple power supplies before. Comparison of the currents revealed that the gain with the AVD is much higher. Adjusting of the voltages with the multiple power supplies to match the gain of the AVD yielded the same shape. Since this overshoot (see 25) is not expected, there had to be another issue with the detector besides the protection circuit.

The reason for this behavior was found to be improper grounding of the picoammeter. It appeared that the ground level of the pad plane was different from the reference ground level of the device which lead to this behavior, probably due to charging up effects in

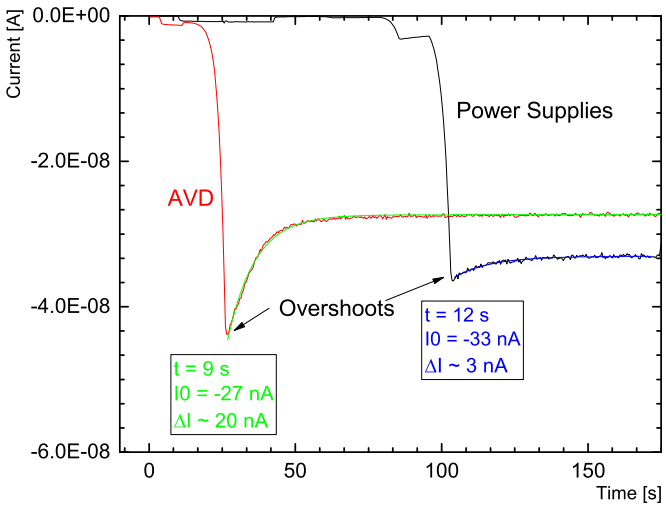

Figure 25: Overshoots observed for AVD (red) and multiple power supplies (black) with simple exponential fits.

the picoammeter. Also the induction gap was changed from 3 mm to 2 mm to match the nominal settings in the TDR. After these issues were solved some measurements were done for both setups, AVD and multiple power supplies. During one of these measurements, the air conditioning in the lab was turned off on purpose to study the dependence of water content and temperature. Hence, the temperature increased up to 29°C. It was observed that the water content of the gas followed the temperature as shown in figure 26.

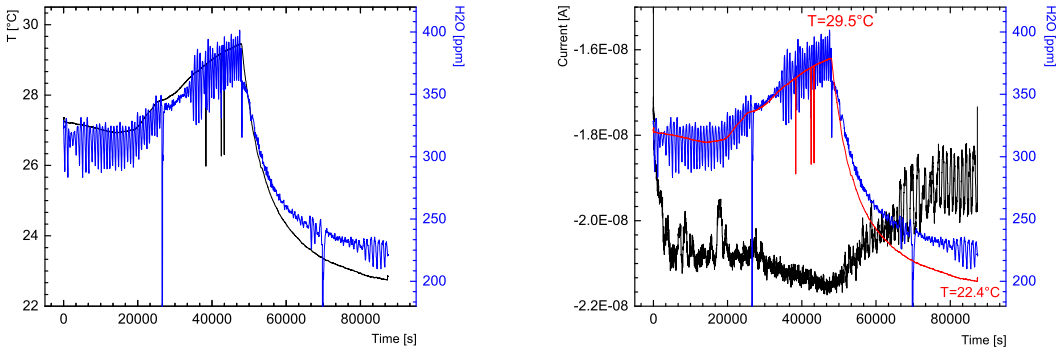

Figure 26: Left: Temperature and H_2O content of the gas; right: same plot with current on pad plane.

The plot on the right additionally shows the current on the pad plane. At the beginning of the measurement, the current is very unstable, which can not be explained by changes in temperature and water. One reason might be a permanent change of the range of the picoammeter, since the current fluctuated around the value where an automatic change of range is triggered. But with increasing temperature also the water content and the current increase. Since it is reasonable to assume that for water contents of around 300 ppm the surface of the polyimide inside the holes is saturated. The increase of current is

therefore most probably due to an increase of the gas density T/p. At the end, after the decrease of the temperature, the current again shows large fluctuations which might also be explained by the change in range of the picoammeter. These measurements nicely confirm the dependence of the water content on the temperature.

After the lab was air conditioned again, measurements with different ramps speeds and safe voltages were done for both, AVD and multiple power supplies, in order to optimize the ramp time and in the assumption that higher safe voltage leads to less discharging during the cool down time. These measurement are done by measuring 5 minutes and letting the detector cool down for 5 minutes.

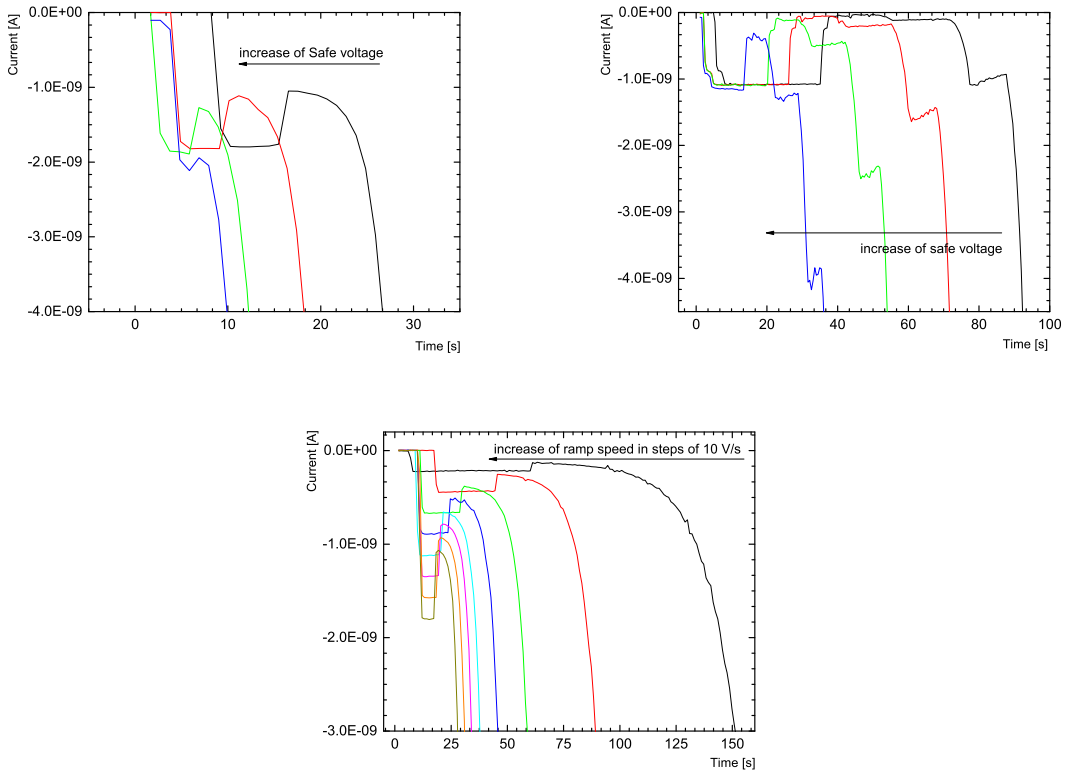

Figure 27: Ramp up behavior for different ramp speeds (bottom) and different safe settings (top left AVD, top right multiple power supplies).

The top two plots in figure 27 show the behavior at the beginning of the ramp for different safe settings for the AVD on the left and multiple power supplies on the right. The safe settings increase from right to left: 50% for the black line to 80% for the blue line in steps of 10%. However, the ramp speed for the AVD was 80 V/s and for the multiple power supplies 20 V/s. Further, the AVD ramps all voltages at the same time whereas the power supplies follow a specific ramping order as mentioned above and therefore the different voltages are delayed. Still, for both plots one can observe a small increase of the current which is due to induced charges on the pad plane. A soon as the voltage for GEM4 bottom is reached the current decreases again until the amplification starts. For the setup with power supplies more steps like this are visible due to delay of the start of ramp of the different voltages. The last step shows the point where the voltage across GEM2 is fully

ramped but the voltage across GEM1 is still to low for amplification.
The plot on the bottom of figure 27 shows ramps with different ramp speeds for the AVD, starting at 10 V/s (black) up to 80 V/s (brownish) starting at 50% of ready voltage. For this, one finds, besides the decreasing duration of the induced current, also a higher current. The overall shape is the same, though.
These measurements yield a maximum safe setting of about 80% of the ready voltages and a show that the ramp speed can not be increased arbitrarily. For further measurements a safe setting of 75% and a ramp speed of 30 V/s for the setup with multiple power supplies are chosen.

4.5. Final measurements with Ar-CO_2 (70-30)

The final measurement, after all issues with the detector were solved, were again done with the Ar-CO_2 premixed gas mixture which is cheaper and shows the same behavior in terms of amplification. For this series of measurements the safe settings were 75% of the ready voltages, which are shown in table 3 as *Ar-CO_2 new*. The ramp speeds were 20 V/s for up and 30 V/s for down and the measuring time interval was changed to 5 s some time after the ramp was finished. The duration of the measurements was 4 h as far as it was possible and the cool down time was increased between measurements starting from one hour up to 12 hours and another measurement with 17 hours of cool down time. An example of the current behavior at ramp is shown in figure 28. One can see that after the ramp is finished after about 70 seconds the current keeps increasing with a reciprocal exponential shape. Note, that this measurement was over more than 4 hours. The overall trend is the mirrored plot of a ramps with improper grounding (see figure 18). Therefore, equation 5 can also be used for fitting. For the time offset t_0 the end of the ramp is chosen.

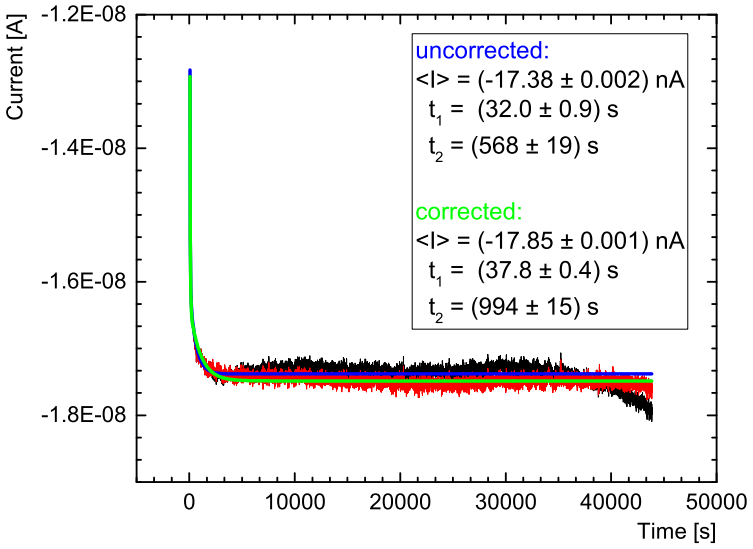

Figure 28: Typical current behavior at ramp after 9 hours of cool down; black uncorrected, red corrected.

Since the measurements were started at different times of the day, some of them were exposed to rather big temperature gradients, especially when they were started in the early morning or the late afternoon. To obtain comparable results the current on the pad plane was corrected for the density, represented by T/p. To quantify this dependence, the current versus $\frac{T}{p}$ has been plotted, which is according to the ideal gas law proportional to the gas density. In theory, this dependence is linear with slope m. The idea of the correction is to make m as small as possible, in the ideal case one would find $m = 0$, which means there is no correlation between current and gas density. To do so, a simple linear function has been fitted to the plot shown on the right in figure 29. The left plot shows all measured data points. For the correction, only the ones after the ramping and after the charging-up are of interest, since during the former processes it is obvious that the current changes, even without change in T/p. After choosing the right interval, the fit is done according to the following equation:

$$I_{pp}^{corr} = I_{pp} - m\left(\frac{T}{p} - \left\langle\frac{T}{p}\right\rangle\right) + \Delta I \quad , \tag{6}$$

where pp stands for pad plane, $\langle\ \rangle$ represents the mean value, and ΔI is an offset that has to be added, since the equation will only twist the straight line around its mean value, which will prevent it from matching the current outside of the interval chosen for the correction. The effect of the correction is shown in red in figure 29. The example also shows the difference between the two ramp schemes. Figure 28 shows the ramp for all power supplies from 75% of the ready voltage, whereas the plot in figure 29 shows the ramp for only the voltage across the first GEM while the others were kept at their nominal voltages. One can see that the current becomes flat after applying this density correction. For some plots, a periodic pattern can be observed even after the correction. An example for this is shown in figure 30.

This might result from a low gas pressure in the gas line. Due to this, the gas flow could be inconstant, which means, when a bigger amount of gas is flushed into the chamber, the

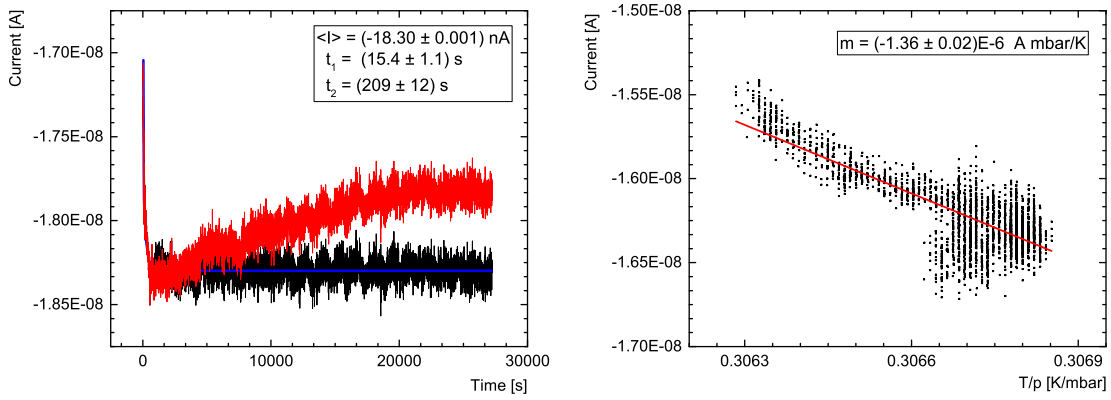

Figure 29: Effect of the correction (right), black corrected, red uncorrected; Current versus T/p plot for correction.

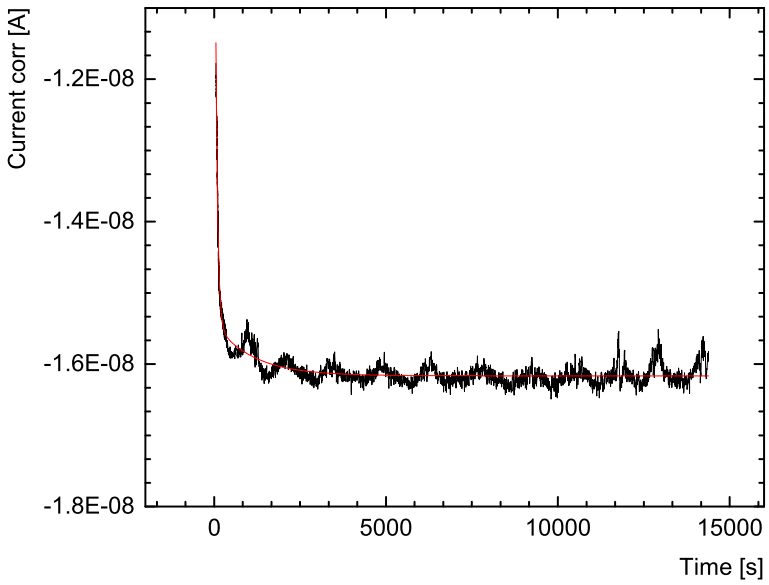

Figure 30: Corrected current on pad plane after 3 h of cool down; clearly visible are oscillations during the whole measurement.

current goes up and vice versa. Again, a fit is done as before, where one notices that these oscillations do not affect the fit, though. Only if an oscillation starts at the transition from the first to the second exponential in equation 5, some problems with the fit might occur. Again, the fit yields two time constants which are both plotted versus the cool down time. Figures 31 and 32 show these plots. The first one shows τ_1 against the cool down time and one can see that there is no obvious dependence. The trend is a straight line with slope zero. The second one consequently shows τ_2 also plotted against the cool down time. The plot shows large excursions of τ_2, but hardly a slight decrease with increasing cool down can be observed. Both plots show the results after the correction was applied. The time constants obtained before the correction was applied are shown in figure 33. As can be seen, some measurements show extreme values or error bars which is due to bad fits or unexplainable changes in the current. These measurements were done a second time to try to reproduce them and see if the first measurements were artifacts or if there is something to it. In the repeated measurement, they could not be reproduced, but follow the trend observed in other measurements. Still, they are shown in the plots. The mean value of τ_2 is in the order of 12 minutes.
In addition, one measurement, where only the voltage across GEM1 was ramped, was done for comparison as mentioned before. It is shown in figure 29 left. The fit yields less than half of the charging up time and about half the ramping time. Also one measurement was done with increased gas pressure to see if the oscillations are due to low pressure and can be eliminated. This plot is shown in figure 34.

The relative current increase during the charging-up can be determined by taking the difference between the current at the end of the ramp and the average current in the

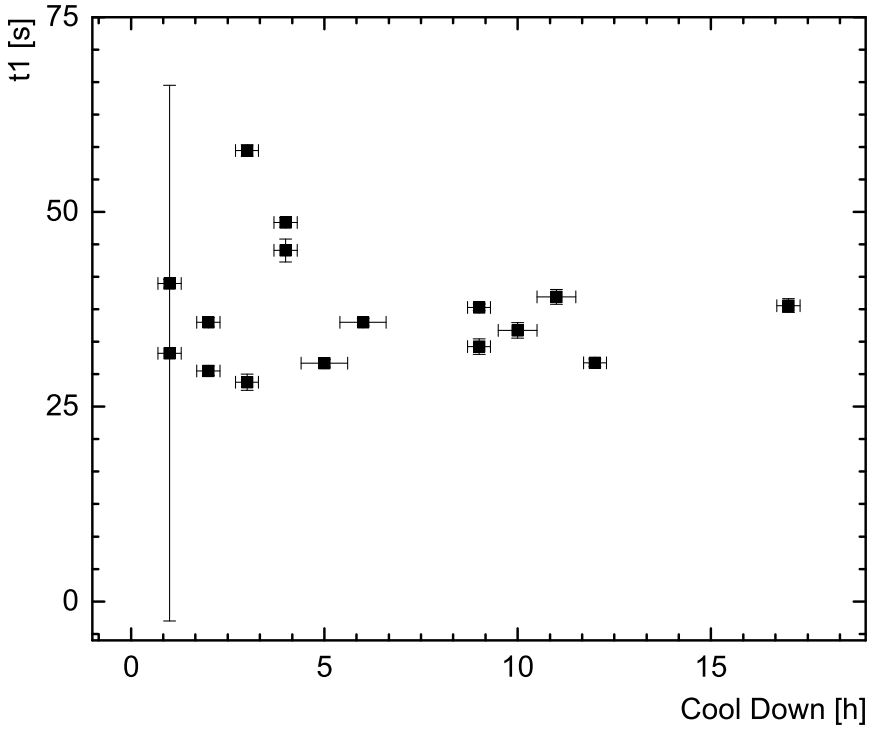

Figure 31: Time constant τ_1 versus cool down time.

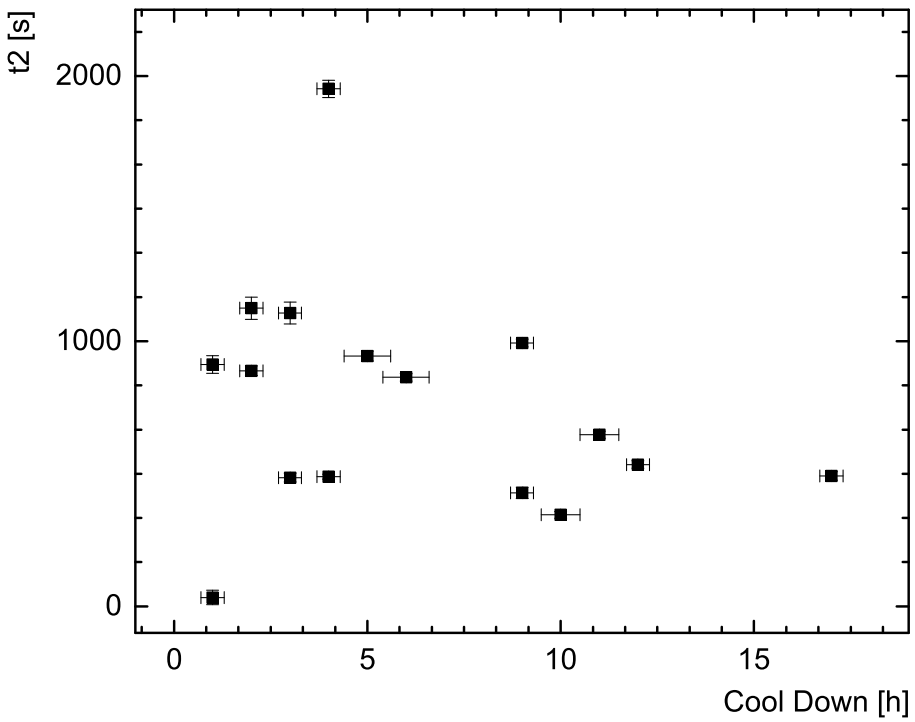

Figure 32: Time constant τ_2 versus cool down time.

steady region divided by the latter. This yields an increase of about 20 to 25% in the above obtained time of roughly 12 minutes. By calculating this increase one notices that the steady current differs by up to 2 nA between different measurements. So far it is not clear, if these differences only originate from differences in ambient parameters or if there is another, not considered effect.
The main results and possible error sources will be discussed in the following chapter.

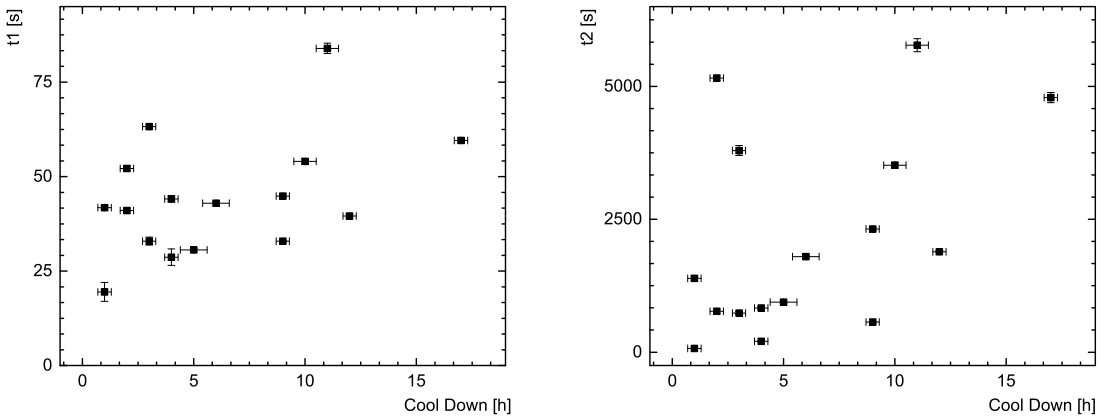

Figure 33: Time constants τ_1 and τ_2 before the correction.

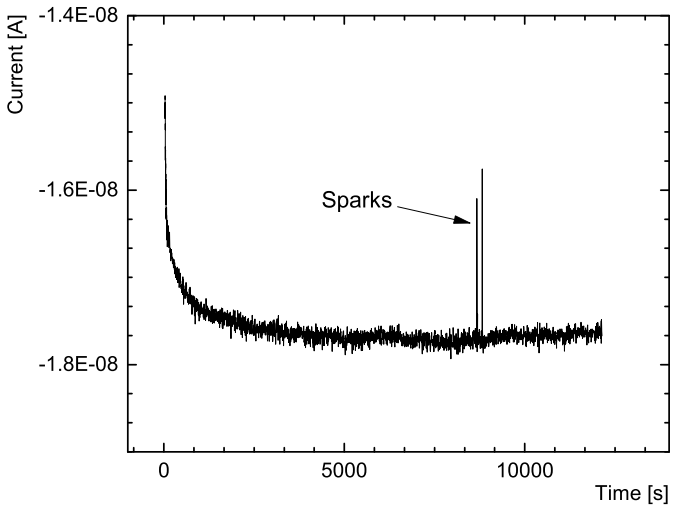

Figure 34: Measurement with increased gas pressure; two small discharges occurred

.

4.6. Results and Discussion

What this thesis mainly yields is shown in figure 32. It can be seen, that the charging up time of the foils is fairly constant, no matter what the cool down time is. If at all, the data shows a decreasing trend with increasing cool down time. Further it came out, that the time constant for charging-up is independent of the duration of the measurement,

which means an equilibrium state is reached at some point. This again means that it does not matter, if the measurement lasts for 4 h or for 10 h, as long as it is longer than the charging-up time itself, which leads to a minimum measurement time of roughly 20 minutes. A proper and working correction for T/p was also applicable. But still, there are some variations in the current on the pad plane that are not understood yet and could not be corrected.
In terms of errors in the measurements and in the plots, it has to be mentioned that none of the data acquired directly via the sensors is given with an error. Due to the very high number of measurements, additional error data would make it unnecessarily complicate to evaluate. Plus, the current itself has a statistical character due to radioactive decay law for the source. For the temperature sensor also statistics would apply, since it seems odd, that the temperature changes multiple times within a few seconds. Same applies for the water content of the gas. The fits then yields such a statistical error, but due to partly very high numbers of datapoints, these errors are small. Nevertheless, they are adopted for further plots. The error for the cool down time, for example, are estimated value, mostly in the order of 10 minutes.

Other sources of errors, that are not quantitatively know, might be the detector box itself. Water diffuses through the walls of the detector and enrich the gas. Also it is unknown how much nylon gas line is attached to the line used in this experiment. Hence, it is not known if a change of water is only due to change in temperature or if there was some enrichment at the nylon lines or even due to a shortly opened line. However, this should not be of great effect on the measurement, since the water content is high enough to assume the Kapton layer is saturated.
Also temperature stability in the copper box is not given. The box has a hole on the top side and the lid could not be completely closed since some cables had to go out. Therefore it is possible, that the temperature inside the box fluctuates due to air drafts caused by people passing by or just due to thermodynamic effects when the box was warmer on the inside that the lab around. The above mentioned influences should be very small, though.

5. Conclusion

To conclude from the results of this thesis, we find that the charging-up time of the GEM foils is nearly independent of the time in safe mode and is in the order of 12 minutes. Further, the measurements yield an overall stable gain after the correction for T/p. However, there are still some dependencies that are not yet understood and that cause for example a partly oscillating current.

The results from these measurements are obtained from a small number of data points and only show a general trend. To really proof the independence of the charging-up time and the cool down time of the chamber further and far more measurements will be needed to be able to rule out statistical fluctuations. Further, theses measurements should be done under more controlled circumstances and under more realistic conditions, like a way lower water content and temperature stability within 1 K. It thus might be possible to eliminate density effects as good as possible and to obtain a better reproducability of the measurements. Also, these measurements could be started and stopped by a program, for better reproducability, too.
Another improvement for these measurements would be to allow a constant gain check by measuring the current on the drift cathode and compare it to the one on the pad plane with known ion backflow.

Another conclusion that can be drawn, is to avoid protection circuits with high leakage currents, since this leads to less stable currents and distorts the gain measurements by up to a factor of two in this particular case.

For practical use in the coming TPC readout, a charging-up time of about 12 minutes and thereby a change in gain of up to 25% will require online correction. For this, the time constant is long enough to allow for this with a reasonable granularity. However, this thesis does not provide any information about the dependence of the charging-up time on the size of the foils, since only $10 \times 10\,\mathrm{cm}^2$ foils were used. Also, further testings maybe able to find some safe settings to lower this time constant. Constrained on ramping the voltage across the first GEM only, the time constant might be less than half, but for this statement not enough data was acquired.

Acknowledgments

First of all I want to thank Prof. Johanna Stachel for giving me the opportunity to work at CERN during this thesis. My special thanks go to Chilo Garabatos who supervised me at CERN, who was always open for discussions and questions and occasionally showed a lot of patience. Further I want to thank the *RD51* collaboration for the warm welcome in their lab. Also, my thanks go to Danilo Vranic, Alexander Deisting, Renato Negrão and Thomas Morhardt for being of help in several different topics and for taking me inside the ALICE solenoid to show me and let me help with small tasks at the actual TPC.

A. Appendix

A.1. Special Relativity

In particle physics mass, momentum and energy are expressed in $\frac{\text{eV}}{c^2}$, $\frac{\text{eV}}{c}$ and eV. This is due to the fact, that the particles are highly relativistic (in most of the time at least). Where these dimensions come from and how the above mentioned quantities relate to one another is given by special relativity[43], postulated in 1905 by Albert Einstein.

The theory of special relativity combines by then two seperated and absolute dimensions: space and time. To put this into equations, four-vectors are used, such as

$$x^\mu = \begin{pmatrix} ct \\ x \\ y \\ z \end{pmatrix}; \quad x_\nu = (ct, x, y, z); \quad g_{\mu\nu} = \begin{pmatrix} 1 & 0 & 0 & 0 \\ 0 & -1 & 0 & 0 \\ 0 & 0 & -1 & 0 \\ 0 & 0 & 0 & -1 \end{pmatrix} \quad \mu, \nu = \{0, 1, 2, 3\},$$

where the left one is a contravariant and the middle one a covariant four vector. The matrix on the right defines the metric. Further a scalar product is defined as follows:

$$a^\mu b_\mu = a_\mu b^\mu = g_{\mu\nu} a^\mu b^\nu = a_0 b_0 - a_1 b_1 - a_2 b_2 - a_3 b_3 \tag{7}$$

Further Einstein postulated the absoluteness of the speed of light and therefore Lorentz transformation has to be applied to transform between two inertial frames:

$$t' = \gamma(t - \beta z); \quad x' = x; \quad y' = y; \quad z' = \gamma(z - \beta t) \tag{8}$$

where $\beta = \frac{v}{c}$, $\gamma = \frac{1}{\sqrt{1-\beta^2}}$ and natural units were used, such that $c = 1$. Eq. 7 then yields the invariance of the square of a four-vector unter Lorentz transformation and is therefore the same in every inertial frame.
Further, we get for the kinetic energy and the momentum[22]:

$$E_{kin} = \frac{mc^2}{\sqrt{1-\beta^2}} = \gamma m c^2 \quad \text{and} \quad \mathbf{p} = \gamma \beta m c \tag{9}$$

and thus for a particle at rest, $\gamma = 1$ and $E = mc^2$; which is Einstein's famous equation about the equivalence between mass and energy.
In particle physics the momentum can be written in a four-vector $p^\mu = (E, \mathbf{p})$. As mentioned above $\mathbf{p}^2$ is independent of the inertial frame. By choosing the center-of-mass system (CMS), the spacial momentum $\mathbf{p}$ is by definition 0 and thus $\mathbf{p}^2 = 0$ and m^2 is the same in all intertial frames, since there is always a frame where $\mathbf{p} = 0$. This yields:

$$m^2 = p^2 = E^2 - \mathbf{p}^2 = E_{CMS}^2 = p_{CMS}^2 = m^2 \tag{10a}$$

$$s = (p_1 + p_2)^2 = (E_1 + E_2)^2 = 4E^2 \text{ for } E_1 = E_2 = E \tag{10b}$$

[22] for completeness c is idicated in green

m is also called the *invariant mass* and $\sqrt{s}$ is the center-of-mass energy.

In a particle collision at $\sqrt{s}$ other particles can be produced (particle-antiparticle-pairs) as long as $2m \leq \sqrt{s}$ holds, where m is the mass of the produced particle. The mechanisms of how particles are produced in collisions are given by the scattering theory [4], which will only be mentioned here for completeness.
Also, the higher the energy in the collision is, the smaller the scales that can be resolved are, which follows from Heisenberg's uncertainty relation:

$$\Delta x \Delta p \geq \frac{\hbar}{2} \tag{11}$$

where Δx is the spacial resolution that can be achieved.

A.2. Figures and Tables

Table 5: Energy loss of muons in argon gas; contributions of different processes to total energ loss; from [44].

Muons in argon gas (Ar)

Z	A [g/mol]	ρ [g/cm^3]	I [eV]	a	$k = m_s$	x_0	x_1	$\overline{C}$	δ_0
18 (Ar)	39.948 (1)	1.662×10^{-3}	188.0	0.19714	2.9618	1.7635	4.4855	11.9480	0.00

T	p [MeV/c]	Ionization	Brems	Pair prod	Photonucl	Total	CSDA range [g/cm^2]
		[MeV cm^2/g]					
10.0 MeV	4.704×10^1	5.687				5.687	9.834×10^{-1}
14.0 MeV	5.616×10^1	4.461				4.461	1.786×10^0
20.0 MeV	6.802×10^1	3.502				3.502	3.321×10^0
30.0 MeV	8.509×10^1	2.731				2.731	6.598×10^0
40.0 MeV	1.003×10^2	2.340				2.340	1.058×10^1
80.0 MeV	1.527×10^2	1.771				1.771	3.084×10^1
100. MeV	1.764×10^2	1.670				1.670	4.250×10^1
140. MeV	2.218×10^2	1.572				1.572	6.731×10^1
200. MeV	2.868×10^2	1.525				1.526	1.062×10^2
242. MeV	3.316×10^2	1.519			0.000	1.520	*Minimum ionization*
300. MeV	3.917×10^2	1.525			0.000	1.526	1.719×10^2
400. MeV	4.945×10^2	1.551	0.000		0.000	1.551	2.369×10^2
800. MeV	8.995×10^2	1.666	0.000		0.000	1.667	4.854×10^2
1.00 GeV	1.101×10^3	1.714	0.000		0.000	1.715	6.037×10^2
1.40 GeV	1.502×10^3	1.791	0.001	0.000	0.001	1.793	8.316×10^2
2.00 GeV	2.103×10^3	1.878	0.001	0.001	0.001	1.881	1.158×10^3
3.00 GeV	3.104×10^3	1.980	0.002	0.001	0.001	1.985	1.675×10^3
4.00 GeV	4.104×10^3	2.054	0.003	0.002	0.002	2.061	2.168×10^3
8.00 GeV	8.105×10^3	2.226	0.007	0.007	0.004	2.244	4.018×10^3
10.0 GeV	1.011×10^4	2.277	0.010	0.010	0.004	2.301	4.897×10^3
14.0 GeV	1.411×10^4	2.349	0.015	0.016	0.006	2.386	6.603×10^3
20.0 GeV	2.011×10^4	2.420	0.023	0.026	0.008	2.477	9.068×10^3
30.0 GeV	3.011×10^4	2.494	0.037	0.046	0.012	2.589	1.301×10^4
40.0 GeV	4.011×10^4	2.542	0.052	0.067	0.016	2.678	1.681×10^4
80.0 GeV	8.011×10^4	2.647	0.118	0.161	0.032	2.959	3.098×10^4
100. GeV	1.001×10^5	2.677	0.153	0.212	0.039	3.083	3.760×10^4
140. GeV	1.401×10^5	2.721	0.225	0.318	0.055	3.319	5.010×10^4
200. GeV	2.001×10^5	2.764	0.338	0.485	0.078	3.666	6.729×10^4
300. GeV	3.001×10^5	2.810	0.532	0.766	0.117	4.225	9.268×10^4
400. GeV	4.001×10^5	2.842	0.732	1.058	0.156	4.787	1.149×10^5
572. GeV	5.723×10^5	2.879	1.085	1.571	0.223	5.759	*Muon critical energy*
800. GeV	8.001×10^5	2.913	1.561	2.258	0.314	7.048	1.833×10^5
1.00 TeV	1.000×10^6	2.935	1.989	2.874	0.395	8.194	2.096×10^5
1.40 TeV	1.400×10^6	2.969	2.847	4.104	0.560	10.480	2.527×10^5
2.00 TeV	2.000×10^6	3.003	4.161	5.985	0.810	13.960	3.022×10^5
3.00 TeV	3.000×10^6	3.043	6.360	9.110	1.240	19.754	3.621×10^5
4.00 TeV	4.000×10^6	3.071	8.592	12.272	1.677	25.613	4.064×10^5
8.00 TeV	8.000×10^6	3.141	17.605	24.995	3.493	49.235	5.171×10^5
10.0 TeV	1.000×10^7	3.164	22.154	31.395	4.427	61.141	5.535×10^5
14.0 TeV	1.400×10^7	3.199	31.236	44.156	6.347	84.938	6.088×10^5
20.0 TeV	2.000×10^7	3.237	44.956	63.386	9.292	120.872	6.677×10^5
30.0 TeV	3.000×10^7	3.281	67.769	95.400	14.391	180.841	7.349×10^5
40.0 TeV	4.000×10^7	3.312	90.675	127.504	19.616	241.108	7.826×10^5
80.0 TeV	8.000×10^7	3.390	182.502	256.012	41.480	483.384	8.975×10^5
100. TeV	1.000×10^8	3.416	228.520	320.330	52.790	605.056	9.344×10^5

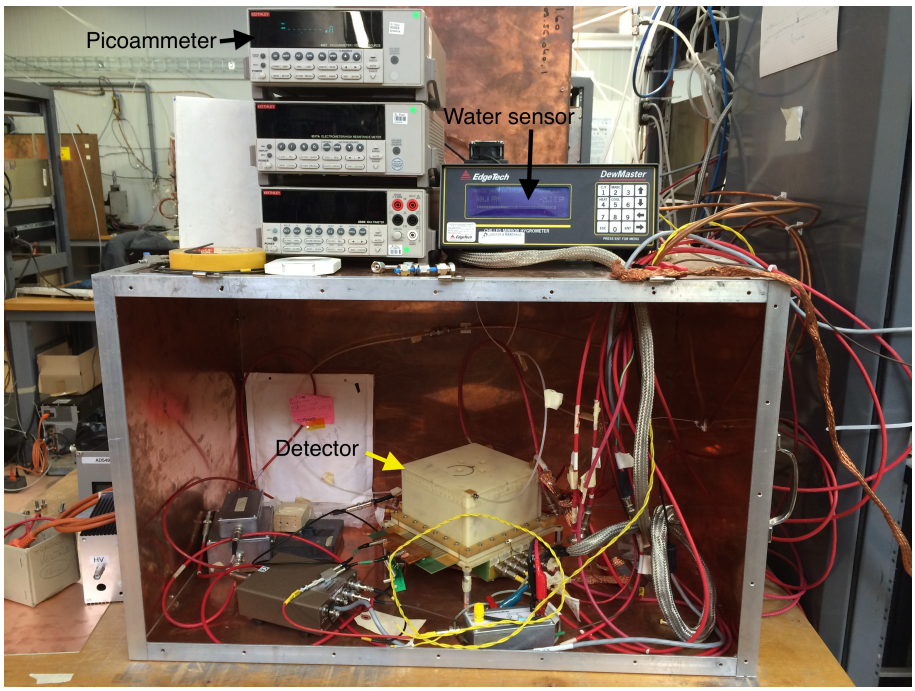

Figure 35: Open copper box with detector inside; picoammeter and water sensor on top.

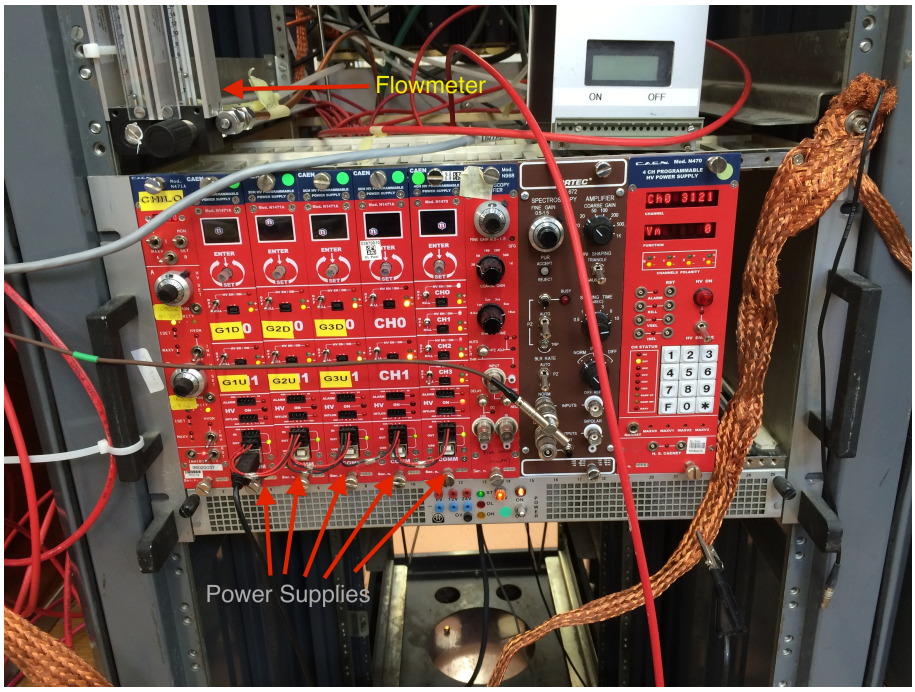

Figure 36: 2 channel (4 channel, resp.) HV power supplies to power the GEMs and the drift field; flowmeter to control gas flow through the detector; copper cable as GND connection.

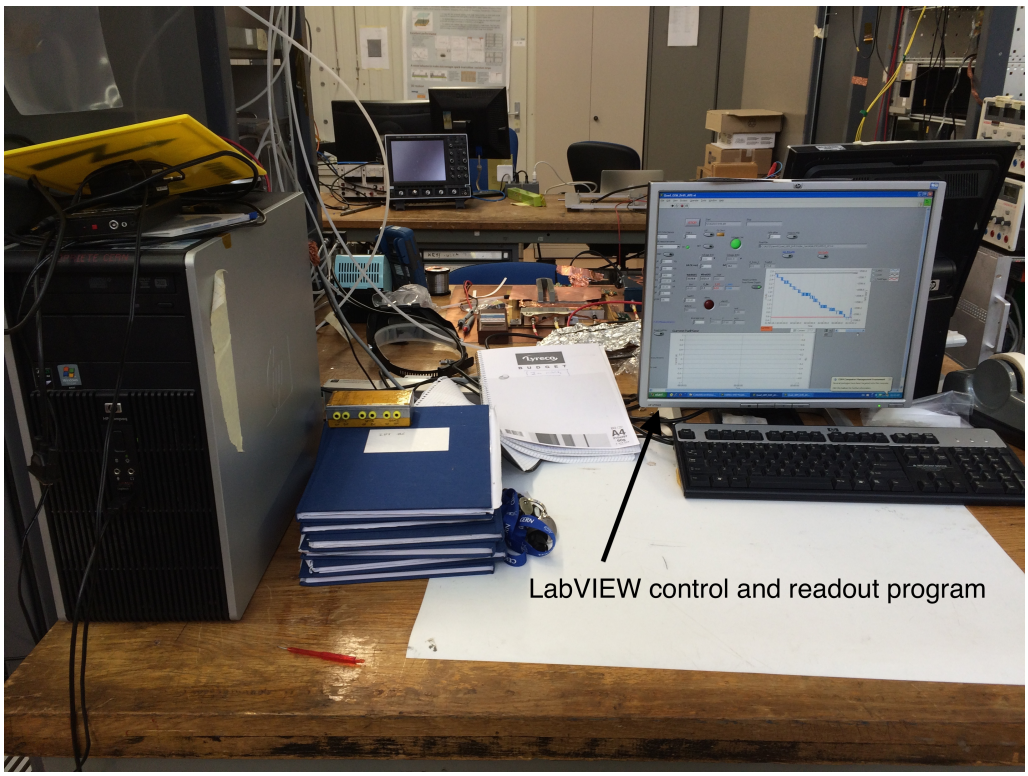

Figure 37: Computer with USB connection to picoammeter, T/p/H_2O-sensor and power supplies; *LabVIEW*™ program for control, readout and live plots.

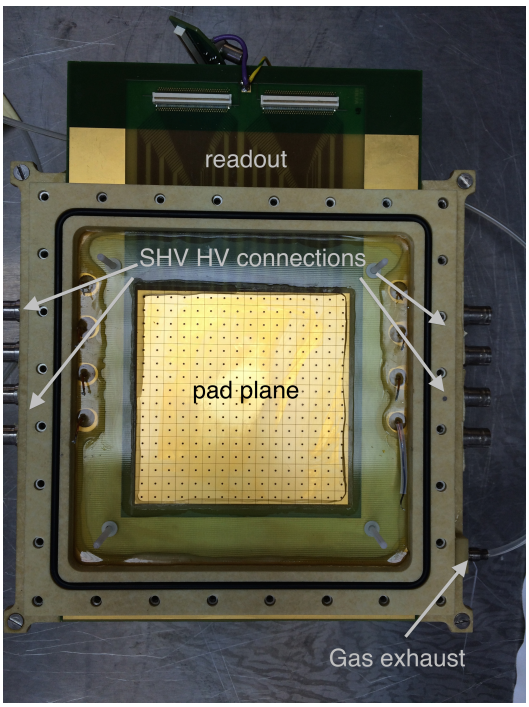

Figure 38: Look on the pad plane from top; SHV HV connetions on both sides to apply voltage to the foils, exhaust gas is analysed for water content.

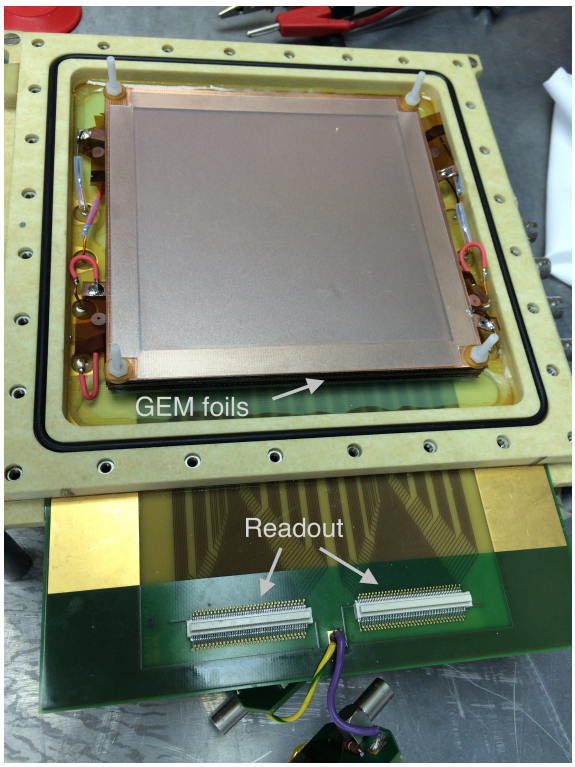

Figure 39: GEM stack and pad plane readout (pad plane below foils, unvisible); milky cover on the top GEM foil for protection.

A.3. Acronyms

ALICE	A Large Ion Cillider Experiment
ATLAS	A Toroidal LHC ApparatuS
AVD	Active Voltage Divider
CERN	European Organization for Nuclear Research
CMS	Compact Muon Solenoid
EMCAL	ElectroMagnetic CALorimeter
FEE	Front End Electronics
GEM	Gas Electron Multiplier
GND	GrouND
HMPID	High Momentum Particle IDentification
HV	High Voltage
IBF	IonBackFlow
IROC	Inner ReadOut Chamber
ITS	Inner Tracking System
LEIR	Low Energy Ion Ring
LINAC	LINear-ACcelerator
LHC	Large Hadron Collider
LHCb	Large Hadron Collider beauty
LS1	Long Shutdown 1
LS2	Long Shutdown 2
MIP	Minimum Ionizing Particle
MPGD	MicroPattern Gaseous Detector
MWPC	Multi-Wire Proportional Chamber
OROC	Outer ReadOut Chamber
PCB	Printed Circuit Board
PHOS	PHoton Sprectrometer
PID	Particle IDentification
PS	Proton Synchrotron
PSB	Proton Synchroton Booster
QCD	Quantum ChromoDynamics
QGP	Quark-Gluon-Plasma
RFQ	Radio Frequence Quadrupole
S, SP, MP, LP	Standard, Small Pitch, Medium Pitch, Large Pitch
SM	Standard Model (of particle physics)
SPS	Super Proton Synchroton
TDR	Technical Design Report
TOF	Time Of Flight
TPC	Time Projection Chamber
TRD	Trasition Radiation Detector

References

[1] G. Lemaître. Expansion of the universe, A homogeneous universe of constant mass and increasing radius accounting for the radial velocity of extra-galactic nebulae. *Monthly Notices of the Royal Astronomical Society, Vol. 91, p.483-490*, March 1931.

[2] RD51 Collaboration. URL:http://rd51-public.web.cern.ch/RD51-Public/Welcome.html, 2010. Accessed: 2015-07-16.

[3] RD51 Collaboration et al. Development of Micro-Pattern Gas Detector Technologies. Technical report, CERN-LHCC-2008-011/LHCC-P-001, August 2008.

[4] B. Povh, K. Rith, C. Scholz, F. Zetsche, and W. Rodejohann. *Teilchen und Kerne*. Springer Spektrum, Berlin, Heidelberg, 2014. 9. Aufl.

[5] "MissMJ". Standard Model of Particle Physics. URL:http://commons.wikimedia.org/wiki/File:Standard_Model_of_Elementary_Particles.svg#/media/File:Standard_Model_of_Elementary_Particles.svg, June 2006. Accessed: 2015-05-05.

[6] M. Stephanov. QCD phase diagram and the critical point. *arXiv preprint hep-ph/0402115*, 2004.

[7] V. Lizardo and B. Espagnon. *Inclusive J/ψ production measurement in Pb-Pb collisions at $\sqrt{s_{NN}}$ = 2.76 TeV with the ALICE Muon Spectrometer*. PhD thesis, Orsay, 2013. presented 06 September 2013.

[8] Communication Group. CERN faq - LHC the guide, February 2009.

[9] CERN Webpage. Large Hadron Collider. URL:http://home.web.cern.ch/topics/large-hadron-collider. Accessed: 2015-04-20.

[10] CERN Webpage. Linear Accelerators. URL:http://home.web.cern.ch/about/accelerators/linear-accelerator-2. Accessed: 2015-04-24.

[11] H. Wiedemann. *Particle accelerator physics; 3rd ed.* Springer, Berlin, 2007.

[12] O. Brüning et al. *LHC Design Report*, volume 1-3. CERN, Geneva, 2004.

[13] M.E. Angoletta et al. PSB LLRF renovation: Initial beam tests of the new digital beam control system. *CERN*, Jun 2009.

[14] J.-P. Burnet et al. *Fifty years of the CERN Proton Synchrotron: Volume 1*. CERN, Geneva, 2011.

[15] CERN Webpage. The Super Proton Synchrotron. URL:http://home.web.cern.ch/about/accelerators/super-proton-synchrotron. Accessed: 2015-07-02.

[16] ATLAS Group. Expecting the Unknown. URL:http://atlas.ch, 2013.

[17] ATLAS Group. Mapping the secrets of the universe, from the Higgs boson to the unknown. URL:http://atlas.ch, 2014.

[18] L. Taylor. About CMS. URL:http://cms.web.cern.ch/content/about-cms, 08 2011. Accessed: 2015-04-29.

[19] The LHCb Experiment. The LHCb Detector. URL:http://lhcb-public.web.cern.ch/lhcb-public/en/Detector/Detector-en.html, 2008. Accessed: 2015-04-29.

[20] The ALICE Collaboration. *ALICE: Technical proposal for a Large Ion Collider Experiment at the CERN LHC*. LHC Tech. Proposal. CERN, Geneva, 1995.

[21] ALICE Collaboration. URL:http://aliceinfo.cern.ch/Public/en/Chapter2/Chap2Experiment-en.html. Accessed: 2015-05-13.

[22] M. J. Kweon. The Transition Radiation Detector for ALICE at LHC. *Nucl. Phys. A*, 830(arXiv:0907.3380):535c–538c. 4 p, July 2009.

[23] E. Casula and A. De Falco. *Low mass dimuon production with the ALICE muon spectrometer*. PhD thesis, Cagliari U., March 2014. Presented 16 April 2014.

[24] The ALICE Collaboration. Upgrade of the ALICE Time Projection Chamber. Technical Report CERN-LHCC-2013-020. ALICE-TDR-016, CERN, Geneva, October 2013.

[25] F. Sauli. *Gaseous radiation detectors: fundamentals and applications*. Cambridge monographs on particle physics, nuclear physics and cosmology. Cambridge Univ. Press, Cambridge, 2014.

[26] Alme et al. The ALICE TPC, a large 3-dimensional tracking device with fast readout for ultra-high multiplicity events. *Nucl. Instrum. Methods Phys. Res., A*, 622(arXiv:1001.1950):316–367. 55 p, January 2010.

[27] private communication with Danilo Vranic, June 2015.

[28] W. Blum, W. Riegler, and L. Rolandi. *Particle detection with drift chambers; 2nd ed.* Springer, Berlin, 2008.

[29] J. Beringer et al. Review of Particle Physics. *Phys. Rev.*, D86:010001, 2012.

[30] A. Sharma and F. Sauli. First Townsend coefficient measured in argon based mixtures at high fields. *Nucl. Instrum. Methods Phys. Res., A*, 334(CERN-PPE-93-50-REV):420–424, 1993.

[31] T. Aoyama. Generalized gas gain formula for proportional counters. *Nucl. Instrum. Methods Phys. Res., Sect. A*, 234(1):125–131, 1985.

[32] C. Grupen and B. Shwartz. *Particle Detectors*. Number 26 in Cambridge monographs on particle physics, nuclear physics, and cosmology. Cambridge University Press, New York, NY, 2nd edition, 2008.

[33] F. Sauli. GEM: A new concept for electron amplification in gas detectors. *Nucl. Instrum. Methods Phys. Res., Sect. A*, 386(2):531–534, 1997.

[34] DuPont. *Kapton - Summary of Properties*, June 2015. Company manual.

[35] Y. Ivaniouchenkov et al. Breakdown limit studies in high-rate gaseous detectors. *Nucl. Instrum. Methods Phys. Res., Sect. A*, 422(1):300–304, 1999.

[36] S. Bachmann et al. Charge amplification and transfer processes in the gas electron multiplier. *Nucl. Instrum. Methods Phys. Res., Sect. A*, 438(2):376–408, 1999.

[37] K.A. Olive et al. Review of Particle Physics. *Chin.Phys.*, C38:090001, 2014.

[38] B. Azmoun et al. A study of gain stability and charging effects in GEM foils. In *Nuclear Science Symposium Conference Record, 2006. IEEE*, volume 6, pages 3847–3851. IEEE, 2006.

[39] F. Simon et al. Development of Tracking Detectors with industrially produced GEM Foils. *Nucl. Instrum. Methods Phys. Res., A*, 572(arXiv:0707.2543):201–202. 6 p, July 2007.

[40] R. Bouclier et al. New observations with the gas electron multiplier (GEM). *Nucl. Instrum. Methods Phys. Res., A*, 396(CERN-PPE-97-032):50–66. 25 p, March 1997.

[41] private communication with Hans Müller, May 2015.

[42] M.-M. Bé et al. *Table of Radionuclides*, volume 3 of *Monographie BIPM-5*. Bureau International des Poids et Mesures, Sèvres, France, 2006.

[43] M. Thomson. *Modern particle physics*. Cambridge University Press, Cambridge, U.K., 2013.

[44] Particle Data Group. Atomic and Nuclear Properties of Materials. `URL:http://pdg.lbl.gov/2014/AtomicNuclearProperties/`, August 2014.

[45] private communications with Chilo Garabatos, March - July 2015.

Erklärung

Ich versichere, dass ich diese Arbeit selbstständig verfasst und keine anderen als die angegebenen Quellen und Hilfsmittel benutzt habe.

Heidelberg, den 29. März 2016,